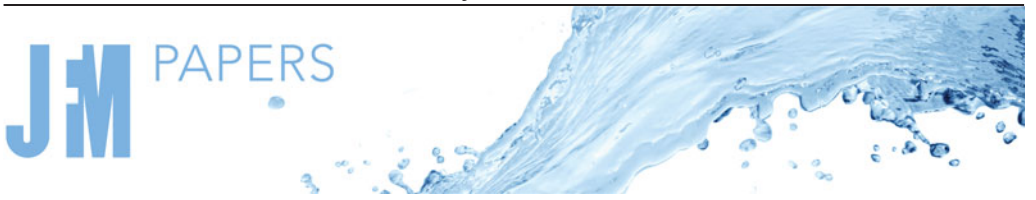
J. Fluid Mech. (2021), *vol*. 915, A114, doi:10.1017/jfm.2021.68



A CFD data-driven aerodynamic model for fast and precise prediction of flapping aerodynamics in various flight velocities

Xuefei Cai[1,2], Dmitry Kolomenskiy[2,3], Toshiyuki Nakata[2] and Hao Liu[1,2,†]

[1]Shanghai Jiao Tong University and Chiba University International Cooperative Research Center (SJTU-CU ICRC), Shanghai Jiao Tong University, 800 Dongchuan Road, Minhang District, Shanghai 200240, PR China

[2]Graduate School of Engineering, Chiba University, 1-33 Yayoi-cho, Inage-ku, Chiba 263-8522, Japan

[3]Global Scientific Information and Computing Center, Tokyo Institute of Technology, 2-12-1, Ookayama, Meguro-ku, Tokyo 152-8550, Japan

(Received 27 April 2020; revised 11 January 2021; accepted 15 January 2021)

Precise prediction of unsteady flapping aerodynamics in insect flight is of potential importance in the analysis of maneuverability and flight control. While the quasi-steady model is a cheap while reasonable tool, accurate evaluation of unsteady dynamic effects in complex flight behaviours remains a challenge. Here we develop a computational fluid dynamics (CFD) data-driven aerodynamic model (CDAM), which is informed by high-fidelity CFD simulations using overset meshes to enable the precise and fast prediction of both cycle-averaged and transient aerodynamic force, torque and power with various flying motions and wing kinematics. The CDAM comprises a quasi-steady model for flapping wings and an aerodynamic model for a moving body. The least square method and a surrogate method are employed to achieve aerodynamic coefficient fitting through training using a CFD database. With comparison to CFD test data, the CDAM is validated to be capable of accurately evaluating the aerodynamic force, torque and power of a wing-body bumblebee model in various flight velocities. A genetic optimization algorithm embedded with CDAM is proposed to determine trimmed states for forward flight through adjusting wing kinematics, indicating that bumblebees likely fly in a minimized mass-specific aerodynamic power consumption. The CDAM is further applied to proportional-derivative-based longitudinal flight control of bumblebee hovering, with the control parameters optimized by Laplace transformation and the root locus method, which is implemented consistently in both CDAM and CFD environments. Our results demonstrate that CDAM provides a versatile tool to achieve fast and precise aerodynamical prediction for flying insects in various flight behaviours.

Key words: flow–structure interactions, swimming/flying

† Email address for correspondence: hliu@faculty.chiba-u.jp

© The Author(s), 2021. Published by Cambridge University Press

https://doi.org/10.1017/jfm.2021.68 Published online by Cambridge University Press

1. Introduction

Accurate evaluation of aerodynamic forces that act on a flying insect is a key issue in the analysis of its flight behaviour (Liu *et al.* 2016*b*). Mathematical modelling of this problem counts a hundred years of history that probably begins with the work of Demoll (1918) who attempted to use empirical formulae based on experiments with flat plates. Hoff (1919) pointed out the resemblance between the flow of a flapping insect and a propeller, and suggested using dynamic similarity formulae. Those calculations provided only an order-of-magnitude estimate, since a simple steady-flow formula was used. Hoff's approach, nonetheless, became foundational for the quasi-steady aerodynamic modelling, and later studies improved upon this simple idea by including more terms in the expressions for the aerodynamic forces to account for unsteady, three-dimensional and other effects (see, e.g. Osborne 1951; Weis-Fogh 1973; Ellington 1984). Development of synchronous high-speed videography has enabled sophisticated quasi-steady calculations that include realistic three-dimensional motions. At the same time, high-fidelity numerical simulations by solving the Navier–Stokes equations (Liu & Kawachi 1998; Liu *et al.* 1998; Liu 2009; Engels *et al.* 2016*b*; Nguyen *et al.* 2016; Cheng & Sun 2018; Ishihara 2018; Zhang, Hedrick & Mittal 2019; Oh *et al.* 2020) and dynamically scaled robotic experiments (Dickinson, Lehmann & Sane 1999; Sane & Dickinson 2002; Dickson & Dickinson 2004; Lentink & Dickinson 2009) have been implemented to reveal the flow structures, time-dependent aerodynamic forces, torques and power consumption.

Deeper understanding of the aerodynamics mechanisms of flapping flight is reflected in the structure of the state-of-the-art quasi-steady formulae that typically include the translational terms (Dickinson *et al.* 1999), the added mass term (Sedov 1965) and rotational terms (Pesavento & Wang 2004; Whitney & Wood 2010; van Veen, van Leeuwen & Muijres 2019). The aerodynamic force of a flapping wing at any time point is fully determined, under the quasi-steady assumption, by the instantaneous motion of the wing. It is important to note that, unlike translating airfoils, a flapping wing rotates around the wing hinge, so the incoming flow velocity in the reference frame of the wing is non-uniform. Hence, the blade element method (Osborne 1951; Glauert 1983) is commonly adopted. The wing is divided into a series of small elements in the spanwise direction, and each element is treated as a pitching and heaving airfoil. Then, the aerodynamic forces and torques are calculated for each blade element using a two-dimensional quasi-steady model. Finally, the elementary forces and torques are summed up to obtain the total aerodynamic forces and torques on the entire flapping wing.

The diversity of flapping flight systems that exist in nature and appear in biomimetic mechanical devices is so vast that it hardly can be encompassed in one universal quasi-steady model. Instead, the existing models often specialize in a certain flight regime, e.g. hovering (Nabawy & Crowther 2014), focus on selected species, e.g. locust (Jensen & Pringle 1956), beetle (Oh *et al.* 2020), and predict a number of selected quantities of interest, such as the mean lift and power (Nabawy & Crowther 2014), wing pitching moments (Wang, Goosen & van Keulen 2016), etc. The architecture of a quasi-steady model is determined by its intended area of application. Nowadays, these models are often considered as a computationally inexpensive alternative to the more costly Navier–Stokes simulations. They become helpful when a large number of different designs are compared, as in the geometric optimization, of when the long-time evolution of the aerodynamic forces is required for problems such as flight control (Deng, Schenato & Sastry 2006).

The development of the model presented in this paper has been motivated by prospective application in the field of navigation of insects in environments with unsteady aerial conditions. In our earlier work we developed computational fluid dynamic (CFD) models

https://doi.org/10.1017/jfm.2021.68 Published online by Cambridge University Press

of a bumblebee that provide comprehensive information about the airflow, aerodynamic forces and fluid–structure interaction (Engels *et al.* 2016*a*; Ravi *et al.* 2016; Kolomenskiy *et al.* 2019). These models are practical for simulations of relatively short free flight sequences of less than a hundred wing beat periods, but become prohibitively costly beyond that point. Here, we develop on the ideas of Nakata, Liu & Bomphrey (2015) who proposed a methodology for identification of the quasi-steady model coefficients using data from CFD simulations of which overset meshes including one body-fitted mesh, two wing-fitted meshes and a background mesh are adopted to deal with the complex geometry and movements of a winged body (Liu 2009). Such CFD-informed quasi-steady modelling is driven by a compromise between the complexity of the model and its accuracy. Good accuracy requires that the model accounts for strongly nonlinear effects such as wake capture and aerodynamic interference between the wings and the body. Where a general analytical description introducing additional terms in the quasi-steady equations may appear problematic, for the specific task of evaluating the aerodynamic forces and torques it is sufficient to adjust the basic aerodynamic coefficients to match with the CFD results for some selected representative flight conditions, and fill in interpolation tables.

In § 2 of this paper we present the mathematical formulation of our CFD data-driven aerodynamic model, which consists of two different sets of equations for the wings and body, respectively, as described in §§ 2.2 and 2.3. Note that we introduce a new abbreviation, CDAM, which stands for CFD data-driven aerodynamic model. By enrolling the unsteady aerodynamic effects dependent on the flying velocity through the coefficients informed by CFD simulations, CDAM can handle a range of velocity (e.g. hovering, forward, backward, sideways and climbing flight). In § 3 we describe the CFD method, build up a database necessary for the identification of CDAM coefficients, and calculate the interpolation tables of the model. The database covers a three-dimensional domain ranging from $-0.4U_{ref}$ to $0.4U_{ref}$ in the forward/backward direction, $-0.4U_{ref}$ to $0.4U_{ref}$ in the lateral direction, 0 to $0.4U_{ref}$ in the vertical direction. The performance of CDAM is evaluated in § 4. The CDAM gives a precise prediction of the aerodynamic force, torque and power consumption of a modelled bumblebee with a variety of motions and wing kinematics. In § 5 we propose a genetic optimization algorithm embedded with CDAM to search the trim states of forward flight and find a linear relationship between power consumption and body angle and stroke plane angle. In § 6 we propose a proportional-derivative (PD) control strategy treating the position/attitude along with corresponding velocities with the aid of CDAM to optimize the control parameters. Implementation of the developed PD controller in the CFD environment is also studied and compared with that in the CDAM environment. The control results further confirm the validity of CDAM and its suitability for fluid–structure interaction simulation. In § 7 we apply the CDAM on a hawkmoth for comparison to test its limits at high Reynolds numbers.

2. Construction of CDAM

In this section a CDAM is constructed to predict the aerodynamic force, torque and power consumption of a flying bumblebee. It consists of two components: a CFD-informed quasi-steady model for flapping wings and a simplified aerodynamic model for a moving body. The flapping-wing model can account for a variety of flying velocities and wing kinematics which is based on the blade element method. The wings are assumed to be flat and rigid. They are divided into small elements. The quasi-steady model is applied on each element to obtain the aerodynamic force, torque and power which are consequently

https://doi.org/10.1017/jfm.2021.68 Published online by Cambridge University Press

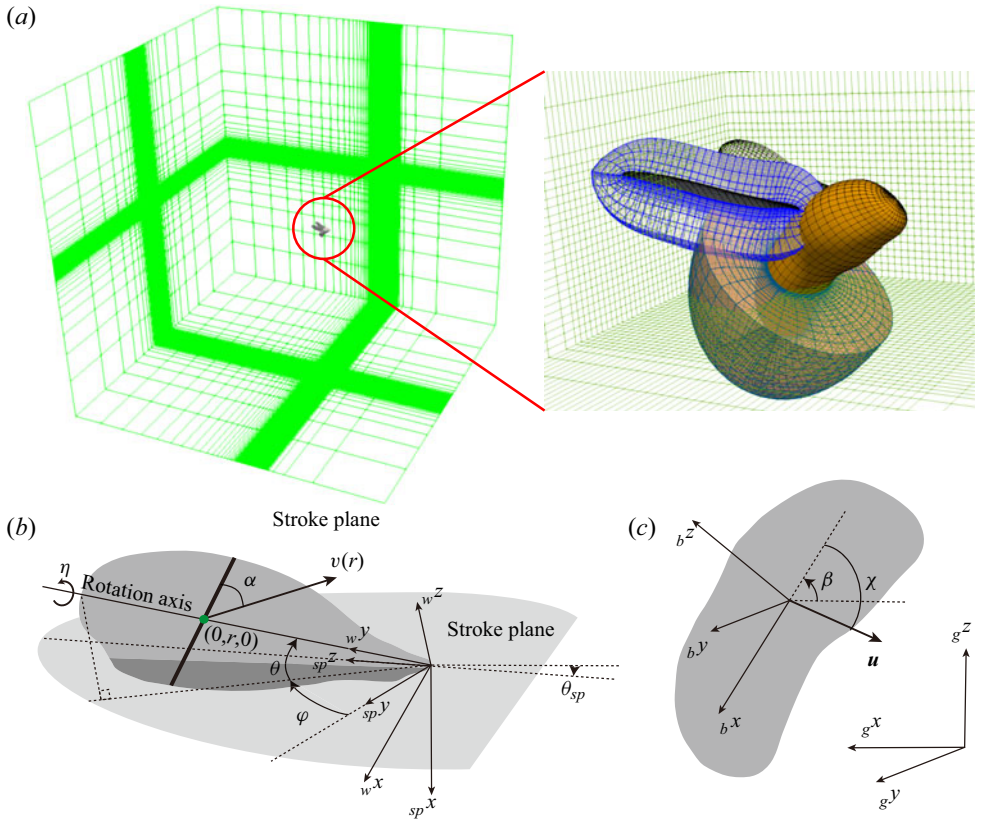


Figure 1. (*a*) An overview of the integrated wing-body model of a bumblebee. (*b*) A sketch of a single wing with the definitions of wing-fixed frame ($_w x$, $_w y$, $_w z$), stroke plane frame ($_{sp}x$, $_{sp}y$, $_{sp}z$), stroke plane angle θ_{SP}, positional angle φ, elevation angle θ and feathering angle η. Here $\boldsymbol{v}(r)$ represents the velocity of a blade element on the wing with the distance r to the wing base and α represents the corresponding angle of attack. (*c*) A sketch of the body with the definitions of body-fixed frame ($_b x$, $_b y$, $_b z$), ground frame ($_g x$, $_g y$, $_g z$) and body angle β. Here $\boldsymbol{u}$ represents the velocity of the body and χ represents the corresponding angle of attack.

summed up over the entire wing. Next, the simplified aerodynamic model for the moving body is established to obtain the lift and drag on the body.

2.1. *Nomenclature and coordinate system*

In the wing model the angle of attack of each element is calculated by identifying the direction of the velocity of each element in the wing-fixed frame of reference. This includes summation of the wing rotation relative to the stroke plane and the body motion relative to the ground. Therefore, the wing velocity and the body velocity need to be transformed into the wing-fixed frame of reference. Similarly, to calculate aerodynamic forces that act on the body, the body velocity needs to be transformed into the body-fixed frame of reference. For these purposes, let us introduce the coordinate transforms between different coordinate frames. As is shown in figure 1, we distinguish between the ground frame, the body-fixed frame, the stroke plane frame and the wing-fixed frame. Table 1 explains the notations and abbreviations used in this paper.

In this study the flapping wing is assumed to be flat, rigid and rotating around the wing base with respect to the stroke plane as shown in figure 1. Therefore, the wing kinematics

https://doi.org/10.1017/jfm.2021.68 Published online by Cambridge University Press

$_g\cdot$	Quantity expressed in ground frame
$_b\cdot$	Quantity expressed in body-fixed frame
$_{sp}\cdot$	Quantity expressed in stroke plane frame
$_w\cdot$	Quantity expressed in wing-fixed frame
$\cdot_x$	Component of a vector in x direction
$\cdot_y$	Component of a vector in y direction
$\cdot_z$	Component of a vector in z direction
θ_{SP}	Stroke plane angle
φ	Positional angle
θ	Elevation angle
η	Feathering angle
β	Body angle
g	Gravity acceleration
α	Angle of attack of flapping wing
χ	Angle of attack of moving body
ρ	Density of air

Table 1. List of notations and abbreviations.

can be defined by the given flapping angles called positional, elevation and feathering angles. The angle θ_{SP} is the stroke plane angle with respect to the horizontal plane. The 'rotation axis' in our terminology is the longitudinal axis of the wing. The positional angle φ is measured between the lateral direction and the projection of the rotation axis on the stroke plane; the elevation angle θ is the deviation angle of the rotation axis from the stroke plane; the feathering angle η is the angular displacement of the wing about the rotation axis. The coordinate transformation matrix $E_{g\to w}$ that converts a vector from the ground frame $(_gx, _gy, _gz)$ to the wing-fixed frame $(_wx, _wy, _wz)$ can be expressed as

$$E_{g\to w} = E_{\theta\to w}E_{\varphi\to\theta}E_{sp\to\varphi}E_{g\to sp}, \tag{2.1}$$

where

$$E_{g\to sp} = \begin{pmatrix} \sin\theta_{SP} & 0 & -\cos\theta_{SP} \\ 0 & 1 & 0 \\ \cos\theta_{SP} & 0 & \sin\theta_{SP} \end{pmatrix}, \quad E_{sp\to\varphi} = \begin{pmatrix} 1 & 0 & 0 \\ 0 & \cos\varphi & \sin\varphi \\ 0 & -\sin\varphi & \cos\varphi \end{pmatrix},$$

$$E_{\varphi\to\theta} = \begin{pmatrix} \cos\theta & \sin\theta & 0 \\ -\sin\theta & \cos\theta & 0 \\ 0 & 0 & 1 \end{pmatrix}, \quad E_{\theta\to w} = \begin{pmatrix} \cos\eta & 0 & -\sin\eta \\ 0 & 1 & 0 \\ \sin\eta & 0 & \cos\eta \end{pmatrix},$$

$E_{g\to sp}$ is the coordinate transformation matrix that converts a vector from the ground frame $(_gx, _gy, _gz)$ to the stroke plane frame $(_{sp}x, _{sp}y, _{sp}z)$ which is coinciding with the wing-fixed frame when φ, θ and η are 0, then the coordinate transformation between the stroke plane frame $(_{sp}x, _{sp}y, _{sp}z)$ and the wing-fixed frame $(_wx, _wy, _wz)$ is

$$E_{sp\to w} = E_{\theta\to w}E_{\varphi\to\theta}E_{sp\to\varphi}. \tag{2.2}$$

Similarly, the coordinate transformation matrix $E_{g\to b}$ that converts a vector from the ground frame $(_gx, _gy, _gz)$ to the body-fixed frame $(_bx, _by, _bz)$ can be expressed as

$$E_{g\to b} = \begin{pmatrix} \cos\beta & 0 & -\sin\beta \\ 0 & 1 & 0 \\ \sin\beta & 0 & \cos\beta \end{pmatrix}, \tag{2.3}$$

https://doi.org/10.1017/jfm.2021.68 Published online by Cambridge University Press

where β is the body angle of a modelled bumblebee. The angular velocity of the wing in the stroke plane frame is

$$
\begin{aligned}
{}_{sp}\boldsymbol{\omega} &= \begin{pmatrix} \dot{\varphi} \\ 0 \\ 0 \end{pmatrix} + E'_{\varphi\to\theta} \begin{pmatrix} 0 \\ 0 \\ \dot{\theta} \end{pmatrix} + E'_{\varphi\to\theta} E'_{\theta\to w} \begin{pmatrix} 0 \\ \dot{\eta} \\ 0 \end{pmatrix} \\
&= \begin{pmatrix} \dot{\varphi} - \sin\theta\dot{\eta} \\ -\sin\varphi\dot{\theta} + \cos\varphi\cos\theta\dot{\eta} \\ \cos\varphi\dot{\theta} + \sin\varphi\cos\theta\dot{\eta} \end{pmatrix}; \qquad (2.4)
\end{aligned}
$$

thus, the angular acceleration is

$$
{}_{sp}\boldsymbol{\xi}_w = \frac{\mathrm{d}_{sp}\boldsymbol{\omega}}{\mathrm{d}t}. \qquad (2.5)
$$

The representative velocity and acceleration of each blade element are defined by the velocity and acceleration sampled along the rotation axis, i.e. at points with coordinates $(0, r, 0)'$ in the wing-fixed frame, as illustrated in figure 1. Thus, the representative velocity in the stroke plane frame can be expressed as

$$
{}_{sp}\boldsymbol{v}(r) = {}_{sp}\boldsymbol{\omega} \times \left(E'_{sp\to w} \begin{pmatrix} 0 \\ r \\ 0 \end{pmatrix} \right). \qquad (2.6)
$$

In addition, if the insect flies in air with a certain velocity ${}_{sp}\boldsymbol{v}_b$, then the absolute velocity of the wing blade element is a sum of the wing velocity relative to the body and the body velocity relative to the ground

$$
{}_{sp}\boldsymbol{v}_w(r) = {}_{sp}\boldsymbol{\omega} \times \left[E'_{sp\to w} \begin{pmatrix} 0 \\ r \\ 0 \end{pmatrix} \right] + {}_{sp}\boldsymbol{v}_b; \qquad (2.7)
$$

thus, the acceleration is

$$
{}_{sp}\boldsymbol{a}_w(r) = \frac{\mathrm{d}_{sp}\boldsymbol{v}_w(r)}{\mathrm{d}t}. \qquad (2.8)
$$

2.2. *Quasi-steady model for a flapping wing*

In the blade element method the wing plate is divided into a series of thin elements, like the one located at $(0, r, 0)'$ as illustrated in figure 1. Each element has its velocity ((2.4) and (2.7)) and acceleration ((2.5) and (2.8)), upon which the quasi-steady model is constructed to calculate the aerodynamic force, torque and power.

The quasi-steady model proposed in this study should give high precision for a range of velocities of the insect (forward/backward velocity, lateral velocity and vertical velocity), that is, this model should be applicable to the three-dimensional velocity space, which we define to be a cuboid ranging from $-0.4U_{ref}$ to $0.4U_{ref}$ in the forward/backward direction, $-0.4U_{ref}$ to $0.4U_{ref}$ in the lateral direction, 0 to $0.4U_{ref}$ in the vertical direction, where U_{ref} is the reference velocity defined in table 2. The forward velocity can affect the lift and drag coefficients (Dickson & Dickinson 2004). The coefficients parameterizing the quasi-steady model in this paper also vary with the velocity of the modelled flying bumblebee. Thus, we construct a CFD database covering a variety of flying velocities and wing kinematics which are discrete points in the three-dimensional velocity space.

https://doi.org/10.1017/jfm.2021.68 Published online by Cambridge University Press

m_b	Body mass	390.99 mg
m_w	Wing mass	0.76 mg
m_t	Mass of bumblebee ($m_b + 2m_w$)	392.51 mg
${}_bI_{yy}$	Moment of inertia of body	7.49×10^{-9} kg m^2
R	Wing length	15.2 mm
${}_b\boldsymbol{R}_h$	Location of wing base	$(6.82, 2.63, 2.76)'$ mm
c_m	Mean chord length	4.1 mm
f	Flapping frequency	136 Hz
Φ	Flapping amplitude	139 deg.
U_{ref}	Reference velocity ($2\Phi Rf$)	10.05 m s^{-1}

Table 2. Morphology of bumblebee.

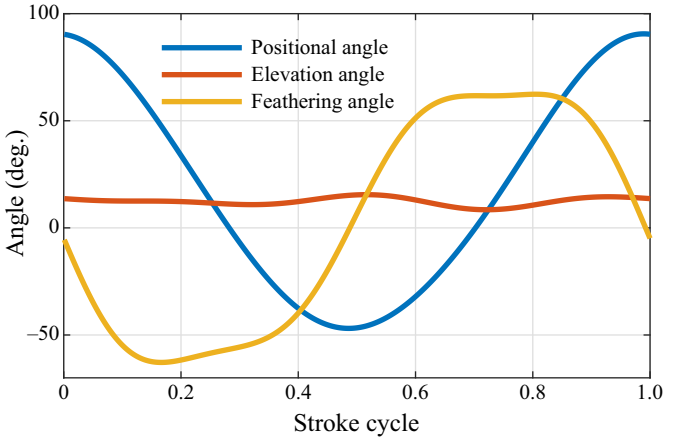


Figure 2. Wing kinematics of a hovering bumblebee (adapted from Kolomenskiy *et al.* 2019).

The wing kinematics of hovering flight are used as a baseline in the study; see figure 2. Then the coefficients are fitted for all the discrete points separately. Finally, the interpolation method is adopted to calculate the coefficients for any point in the three-dimensional velocity space. The construction of the CFD database will be further explained in § 3.

In this study the instantaneous aerodynamic force F_{aero} generated by the flapping wing can be decomposed into five quasi-steady forces based on the blade element method: translational circulation force F_{tc}, rotational circulation force F_{rc}, translational drag F_{td}, rotational drag F_{rd} and force due to added mass F_{am}. The CFD simulation of a flapping-wing insect has shown that the aerodynamic force applied on the flapping wing is mainly normal to the wing surface (Nakata *et al.* 2015) when the Reynolds number is of the order of several hundreds or thousands because the aerodynamic force in the wings is dominated by the pressure. Therefore, the aerodynamic force is assumed to be normal to the wing surface (Sane & Dickinson 2002; Wang *et al.* 2016; Bluman & Kang 2017) in this study, of which only the normal component of the instantaneous aerodynamic force is calculated as a sum of terms, i.e.

$$F_{aero,N} = F_{tc,N} + F_{rc,N} + F_{td,N} + F_{rd,N} + F_{am,N}. \tag{2.9}$$

Previous work on quasi-steady models mainly focused on hovering flight (Sane & Dickinson 2002; Whitney & Wood 2010; Nakata *et al.* 2015; Lee *et al.* 2016), in

https://doi.org/10.1017/jfm.2021.68 Published online by Cambridge University Press

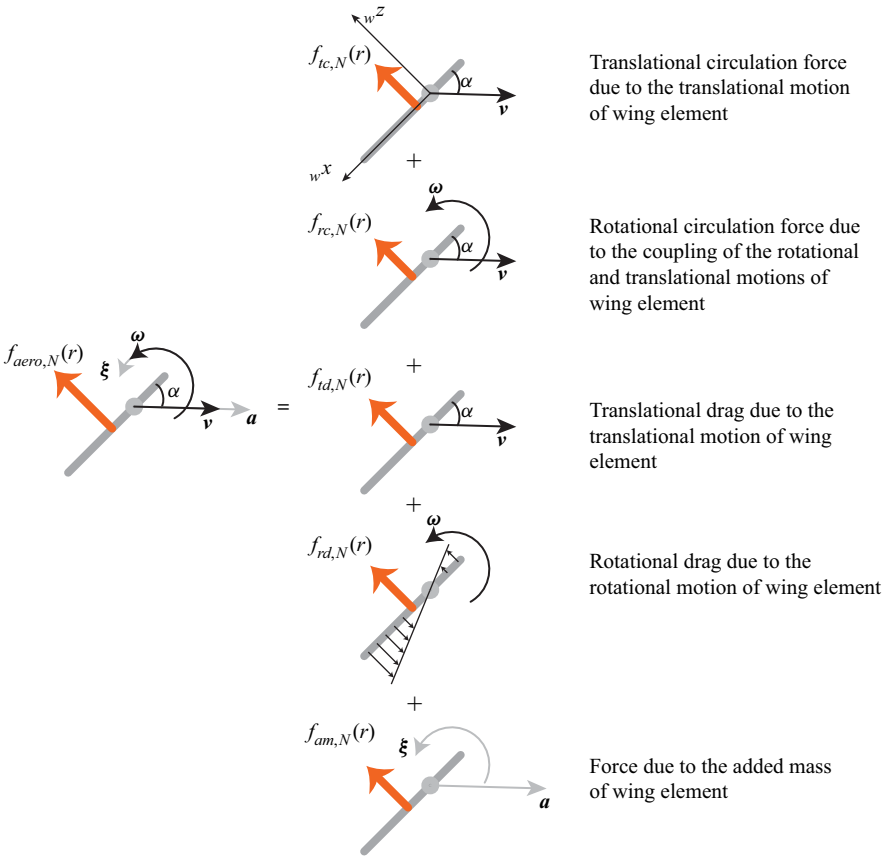


Figure 3. Total aerodynamic force on a wing element can be decomposed into five quasi-steady terms.

which the velocity of each wing blade had zero spanwise component. In our study, the absolute velocity of each wing element includes a non-zero spanwise component due to the body velocity $\boldsymbol{v}_b$. According to Dudley & Ellington (1990*b*) the spanwise component of the velocity does not contribute to the aerodynamic force production. Therefore, only the velocity component normal to the rotation axis is taken into account in the blade element method. Based on the blade element method and zero spanwise velocity assumption, the total quasi-steady aerodynamic force on a wing element is decomposed in five contributions, as shown in figure 3, and the following expressions are used to evaluate these terms (for more details, see appendix A) (Sedov 1965; Pesavento & Wang 2004; Wang 2004; Andersen, Pesavento & Wang 2005; Berman & Wang 2007; Whitney & Wood 2010):

$$f_{tc,N}(r) = -\rho c(r) C_T \cos^2\alpha |_w v_{wn}|_w v_{wn,z}, \tag{2.10}$$

$$f_{rc,N}(r) = -\tfrac{1}{2}\rho C_R \dot{\eta} c^2(r)_w v_{wn,x}, \tag{2.11}$$

$$f_{td,N}(r) = -\tfrac{1}{2}\rho c(r) C_D \sin^2\alpha |_w v_{wn}|_w v_{wn,z}, \tag{2.12}$$

$$f_{rd,N}(r) = -\tfrac{1}{6}\rho C_{rd} |\dot{\eta}| \dot{\eta} (f_l^3(r) + f_t^3(r)), \tag{2.13}$$

$$f_{am,N}(r) = -A_1 \frac{\pi\rho}{4} c^2(r)_w a_{w,z} - A_2 \frac{\pi\rho}{8} (f_l(r) + f_t(r)) c^2(r)_w \dot{\omega}_{w,y}. \tag{2.14}$$

https://doi.org/10.1017/jfm.2021.68 Published online by Cambridge University Press

Here ρ is the density of air, $c(r)$ is the local chordwise length, f_l and f_t are the curves of the leading edge and trailing edge of the wing, ${}_w v_{wn}$ is the velocity component normal to the rotation axis of wing element, $|{}_w v_{wn}|$ represents the magnitude of ${}_w v_{wn}$, C_T is the translational circulation coefficient, C_R is the rotational circulation drag coefficient, C_D is the translational drag coefficient, C_{rd} is the rotational drag coefficient, A_1 and A_2 are the added mass coefficients, η is the feathering angle, α is the angle of attack ranging from 0 to π,

$$\alpha = \arccos\left(-\frac{{}_w v_{w,x}}{|{}_w v_w|}\right). \tag{2.15}$$

Hence, the total aerodynamic force on a blade element is

$$f_{aero,N}(r) = f_{tc,N}(r) + f_{rc,N}(r) + f_{td,N}(r) + f_{rd,N}(r) + f_{am,N}(r), \tag{2.16}$$

which can be written in summation as

$$f_{aero,N}(r) = \sum_{i=1}^{6} I_i f_i(r), \tag{2.17}$$

where

$$I = [C_T, C_R, C_D, C_{rd}, A_1, A_2]^{\mathrm{T}}, \tag{2.18}$$

$$f(r) = \begin{pmatrix} -\rho c(r)\cos^2\alpha |{}_w v_{wn}| {}_w v_{wn,z} \\ -\frac{1}{2}\rho\dot{\eta} c^2(r) {}_w v_{wn,x} \\ -\frac{1}{2}\rho c(r)\sin^2\alpha |{}_w v_{wn}| {}_w v_{wn,z} \\ -\frac{1}{6}\rho|\dot{\eta}|\dot{\eta}(f_l^3(r) + f_t^3(r)) \\ -\frac{\pi\rho}{4} c^2(r) {}_w a_{w,z} \\ -\frac{\pi\rho}{8}(f_l(r) + f_t(r)) c^2(r) {}_w\dot{\omega}_{w,y} \end{pmatrix}, \tag{2.19}$$

and the total aerodynamic forces of the wing can be obtained by integrating (2.10), (2.11), (2.12), (2.13) and (2.14) over the wing,

$$\left.\begin{gathered} F_{tc,N} = \int_0^R f_{tc,N}(r)\,\mathrm{d}r, \quad F_{rc,N} = \int_0^R f_{rc,N}(r)\,\mathrm{d}r, \quad F_{td,N} = \int_0^R f_{td,N}(r)\,\mathrm{d}r, \\ F_{rd,N} = \int_0^R f_{rd,N}(r)\,\mathrm{d}r, \quad F_{am,N} = \int_0^R f_{am,N}(r)\,\mathrm{d}r, \end{gathered}\right\} \tag{2.20}$$

where R is the wing length; thus, (2.9) can be written in summation as

$$F_{aero,N} = \sum_{i=1}^{6} I_i F_i = \sum_{i=1}^{6} I_i \int_0^R f_i(r)\,\mathrm{d}r. \tag{2.21}$$

To close the quasi-steady model for aerodynamic force, coefficients (2.18) must be determined theoretically (Sedov 1965; Fung 2008), experimentally (Dickinson *et al.* 1999; Sane & Dickinson 2002; Andersen *et al.* 2005; Whitney & Wood 2010) or computationally

https://doi.org/10.1017/jfm.2021.68 Published online by Cambridge University Press

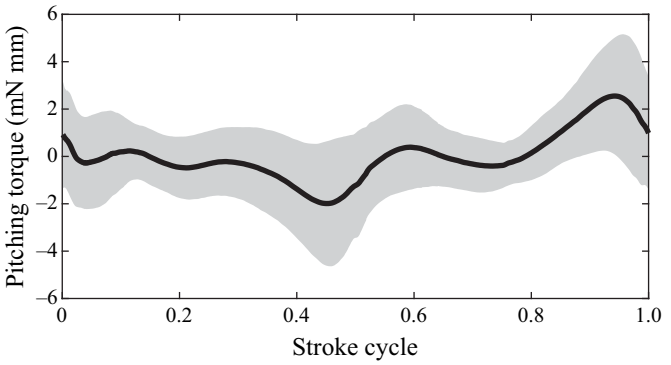


Figure 4. Pitching torque with respect to wing hinge statistically from CFD database over one stroke cycle. Mean value (black line) ± standard deviation (shadow region).

(Pesavento & Wang 2004; Nakata *et al.* 2015; Bluman & Kang 2017). Nakata *et al.* (2015) identified these coefficients for hovering flight by fitting the instantaneous aerodynamic forces from a computational high-fidelity model (Liu & Kawachi 1998; Liu *et al.* 1998; Liu 2009) using the least square method. A similar approach is adopted in this study. It is pointed out by Nakata *et al.* (2015) that increasing the size of input CFD database with different wing kinematics can improve the accuracy of the quasi-steady model.

It is noted that the aerodynamic moment around the rotation axis is below 2 mN mm except for stroke reversal (below 5 mN mm); see figure 4. Following Nakata *et al.* (2015), the cycle-averaged chordwise location of aerodynamic force is fitted from the CFD simulation which is found to be only about $0.03c_m$ away from the 'rotation axis', so the chordwise location of aerodynamic force is assumed to be zero. Hence, the aerodynamic torque with respect to the centre of mass of the modelled bumblebee in the body-fixed frame can be expressed as

$$\begin{aligned} {}_b\boldsymbol{T}_{aero} &= \int_0^R \left[{}_b\boldsymbol{R}_h + E_{w\to b}\begin{pmatrix} 0 \\ r \\ 0 \end{pmatrix} \right] \times \left[E_{w\to b}\begin{pmatrix} 0 \\ 0 \\ F_{aero,N}(r) \end{pmatrix} \right] \mathrm{d}r \\ &= {}_b\boldsymbol{R}_h \times \left[E_{w\to b}\begin{pmatrix} 0 \\ 0 \\ \displaystyle\int_0^R F_{aero,N}(r)\,\mathrm{d}r \end{pmatrix} \right] \\ &\quad + E_{w\to b}\begin{pmatrix} \displaystyle\int_0^R rF_{aero,N}(r)\,\mathrm{d}r \\ 0 \\ 0 \end{pmatrix}, \end{aligned} \tag{2.22}$$

where ${}_b\boldsymbol{R}_h$ is the position of the wing base with respect to the centre of the body in the body-fixed frame. The aerodynamic power required to move the wings through the air is

$$P_{aero} = \int_0^R \begin{pmatrix} 0 \\ 0 \\ F_{aero,N}(r) \end{pmatrix} \cdot {}_w\boldsymbol{v}_w(r)\,\mathrm{d}r = \int_0^R F_{aero,N}(r) \cdot {}_w v_{w,z}\,\mathrm{d}r. \tag{2.23}$$

https://doi.org/10.1017/jfm.2021.68 Published online by Cambridge University Press

2.3. *Simplified aerodynamic model for a moving body*

The contribution of a moving body to the total aerodynamic force and torque cannot be neglected. The aerodynamics of a moving insect body on its own is simpler than the unsteady aerodynamics of flapping wings. However, the interaction between the body and the wings alters the total aerodynamic performance of the body (Yu & Sun 2009; Liu, Dong & Li 2016*a*). The aerodynamic force of the body fluctuates due to the reciprocating motion of the wings, and it is difficult to describe this effect by means of pure theoretical analysis. In this study we construct a simplified aerodynamic model based on the quasi-steady approximation with coefficients fitted to the CFD data. The model consists in the dynamical similarity formulae for the lift

$$ {}_b\boldsymbol{F}_{bd,L} = \rho R^2 C_{bd,L} \sin 2\chi\, |\boldsymbol{u}|^2 (\hat{\boldsymbol{u}} \times (\hat{\boldsymbol{u}} \times {}_b\hat{\boldsymbol{x}})) \tag{2.24} $$

and for the drag

$$ {}_b\boldsymbol{F}_{bd,D} = -\rho R^2 \left[C_{bd,D}(0) \cos^2 \chi + C_{bd,D}\left(\frac{\pi}{2}\right) \sin^2 \chi \right] |\boldsymbol{u}|^2 \hat{\boldsymbol{u}}, \tag{2.25} $$

where $\hat{\boldsymbol{u}}$ is the unit vector in the direction of the body velocity, $C_{bd,L}$ is the lift coefficient, $C_{bd,D}(0)$ and $C_{bd,D}(\pi/2)$ are the drag coefficients that correspond to the angle of attack of the body equal to 0 and $\pi/2$, respectively. The body angle of attack χ varies between 0 and π, and it is calculated as

$$ \chi = \arccos\left(-\frac{{}_b u_x}{|{}_b u|} \right). \tag{2.26} $$

The direction of the lift $\boldsymbol{F}_{bd,L}$ is defined by $(\hat{\boldsymbol{u}} \times (\hat{\boldsymbol{u}} \times {}_b\hat{\boldsymbol{x}}))$ which is normal to the direction of the velocity $\boldsymbol{u}$. Here $\boldsymbol{F}_{bd,L}$, $\boldsymbol{u}$ and ${}_b\hat{\boldsymbol{x}}$ lie in the same plane; ${}_b\hat{\boldsymbol{x}}$ is the unit vector along the x direction in the body-fixed frame. Because the aerodynamic models for the flapping wings and the moving body are independent, $C_{bd,L}$, $C_{bd,D}(0)$ and $C_{bd,D}(\pi/2)$ are independent of wing kinematics and, in addition, are assumed to be independent of the flying velocity. Therefore, $C_{bd,L}$, $C_{bd,D}(0)$ and $C_{bd,D}(\pi/2)$ are constants that are fitted from the CFD training database of the aerodynamic force. Because the body has bilateral symmetry, the centre of the aerodynamic force is assumed to locate on the plane of symmetry which can be expressed in the body frame as $(x_p, 0, z_p)'$. The locations x_p and z_p are also treated as coefficients needed to be fitted from the CFD database. The aerodynamic torque in the body frame is

$$ {}_b\boldsymbol{T}_{bd} = \begin{pmatrix} x_p \\ 0 \\ z_p \end{pmatrix} \times ({}_b\boldsymbol{F}_{bd,L} + {}_b\boldsymbol{F}_{bd,D}). \tag{2.27} $$

3. Construction of the CFD database

3.1. *Bumblebee morphology*

The CFD database will be described using a bumblebee model as an example, which is the main object considered in this paper. The same procedure can be followed to construct other insect models, such as the hawkmoth described in § 7. The mean chord length c_m is treated as a reference length. The body angle and stroke plane angle in hovering are $\pi/4$ and 0, respectively. Detailed morphology parameters are listed in table 2. Wing kinematics of a hovering bumblebee is shown in figure 2. For more information, see Kolomenskiy *et al.* (2019) and Jakobi *et al.* (2018).

https://doi.org/10.1017/jfm.2021.68 Published online by Cambridge University Press

No.	Forward/backward (U_{ref})	Lateral (U_{ref})	Vertical (U_{ref})
1	−0.4	0	0
2	−0.4	0	0.4
3	−0.4	0.4	0
4	−0.4	−0.4	0
5	−0.4	0.4	0.4
6	−0.4	−0.4	0.4
7	0.4	0	0
8	0.4	0	0.4
9	0.4	0.4	0
10	0.4	−0.4	0
11	0.4	0.4	0.4
12	0.4	−0.4	0.4

Table 3. Adopted flight velocities of modelled bumblebee for training data set.

3.2. *Aerodynamic fluid solver*

The flow field around a flying insect is simulated by solving the three-dimensional, incompressible, unsteady Navier–Stokes equations numerically written in strong conservation form for mass and momentum. The CFD solver was first developed by Liu & Kawachi (1998) using the finite volume method in a general formulation of the multi-blocked, structured, overset grid, fortified second-order accurate solutions and was validated repeatedly afterwards (Liu *et al.* 1998; Liu 2002, 2009; Aono & Liu 2006; Shyy *et al.* 2007; Liu & Aono 2009; Liu *et al.* 2010; Nakata *et al.* 2011; Shyy *et al.* 2013). The fortified approach is used to solve the subset equations by adding forcing terms to the Navier–Stokes algorithm in the appropriate flow regions (Van Dalsem & Steger 1986). The governing equation is written in a strong conservation form which is converted into the semi-discrete form by introducing the generalized Reynolds transport theorem and by employing the Gauss integration theorem and discretized in time using a Padé scheme. Here, the CFD simulation of the bumblebee contains four overset grids, i.e. body grid ($37 \times 39 \times 19$), right wing grid ($37 \times 33 \times 11$), left wing grid ($37 \times 33 \times 11$) and background grid ($92 \times 84 \times 68$). Body grid, right wing grid and left wing grid are body-fitted grids; see figures 1(*a*) and 1(*b*). The maximal velocity of 30 m s^{-1} can be reached on the wing tip during the mid-downstroke and mid-upstroke. The time step is 7×10^{-6} s. The minimal size of the grid is also at the wing tip of the 2×10^{-4} m. Thus, the CFL number could be as large as about 1, but typically, it is below 1. To establish the communication between overlapped grids, Newton's method is employed to determine the location of a point inside a cell using tri-linear interpolation (Liu 2009). After three flapping cycles, the flow is fully developed and the quantities are periodic. The periodic state is independent of the starting position.

3.3. *Computational fluid dynamics database acquisition*

As mentioned in § 2, we ran CFD cases in different velocities; see table 3. For each velocity, several CFD cases are run with different wing kinematics; see table 4 to obtain training data. The range of wing kinematics are created by varying the wing beat frequency, as well as the positional and the feathering angle profiles. The elevation kinematics remains unchanged. A total of 71 cases are used to inform the quasi-steady

https://doi.org/10.1017/jfm.2021.68 Published online by Cambridge University Press

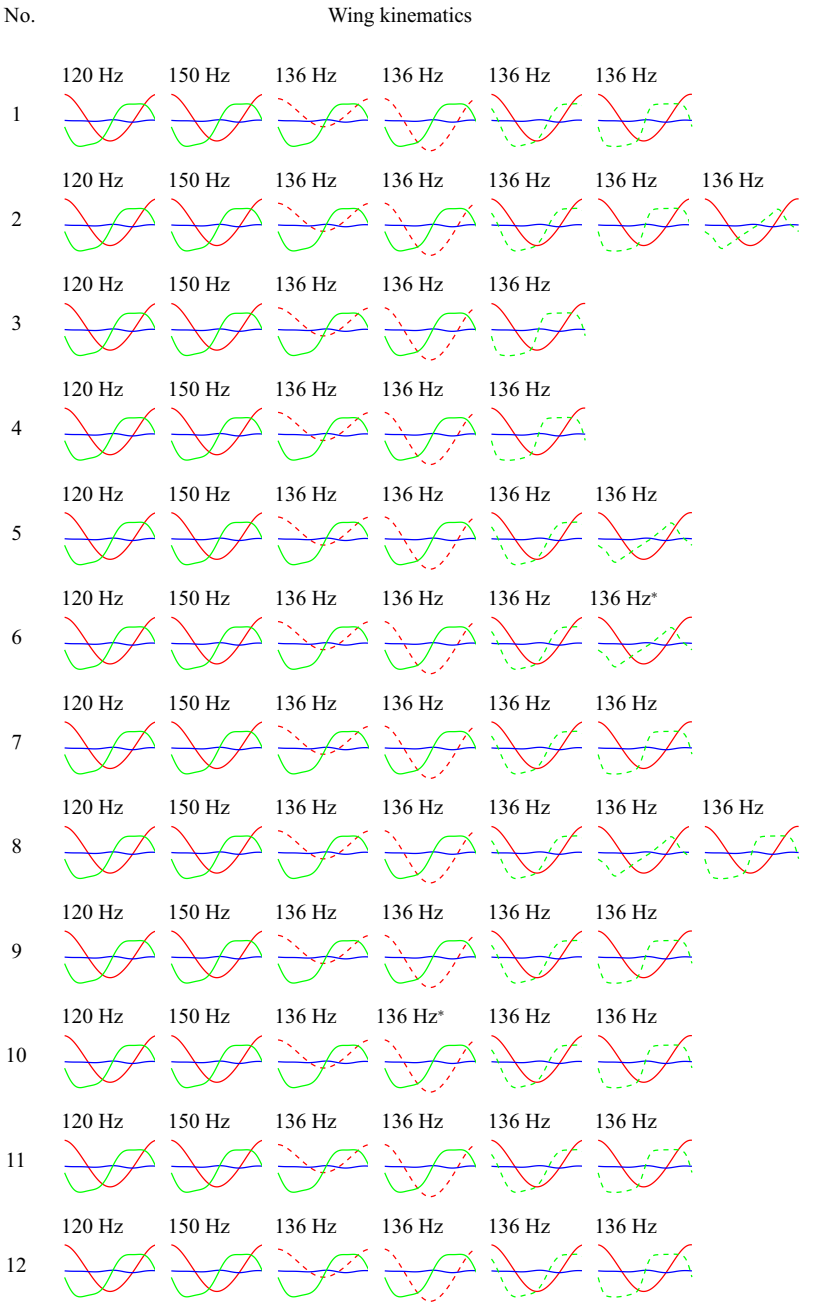


Table 4. Adopted wing kinematics of modelled bumblebee for training data set. The row numbers are corresponding to those in table 3. *Outlier of the least square error of the aerodynamic force normal to the wing surface.

https://doi.org/10.1017/jfm.2021.68 Published online by Cambridge University Press

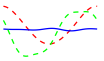
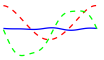
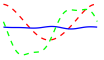
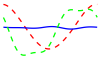
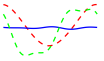
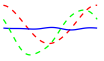
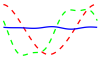
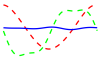
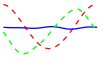
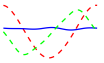
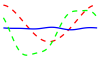
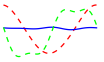
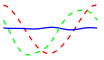
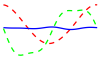
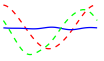
No.	Forward/backward (U_{ref})	Lateral (U_{ref})	Vertical (U_{ref})	Frequency (Hz)	Wing kinematics
1	0.252	−0.286	0.282	147	
2	0.325	−0.062	0.012	123	
3	−0.298	0.332	0.11	147	
4	0.33	0.233	0.018	138	
5	0.105	0.367	0.038	122	
6	−0.177	−0.371	0.277	136	
7	0.037	0.279	0.126	148	
8	0.366	0.347	0.38	148	
9	0.371	0.142	0.013	124	
10	−0.273	0.206	0.175	149	
11	0.376	0.194	0.152	148	
12	0.365	−0.086	0.306	134	
13	−0.011	0.124	0.318	144	
14	0.24	−0.263	0.074	124	
15	−0.321	0.124	0.329	128	

Table 5. Adopted flight velocities and wing kinematics of modelled bumblebee for test data set.

model for a flapping wing and the simplified aerodynamic model for a moving body, which we denote as the training data set. To test the accuracy and generality of the quasi-steady model for flapping wings, simplified aerodynamic model for the moving body and the entire CDAM, 15 more CFD cases with randomly selected flight velocities and wing kinematics were run, forming a test data set; see table 5. Each case can be finished within 20 hours on a computer with 12 cores, hence, it takes about one month to complete the database. Online supplementary material (https://doi.org/10.1017/jfm.2021.68) includes the body grid, the wing grid along with the wing kinematics of the bumblebee model and the results (force, torque and power) of the CFD simulations.

4. Coefficient fitting and accuracy testing

In this section we fit the CDAM coefficients to the CFD training data and test the performance of the model on the CFD test data.

https://doi.org/10.1017/jfm.2021.68 Published online by Cambridge University Press

4.1. *Quasi-steady model for a flapping wing*

In each CFD case the modelled bumblebee begins to flap in quiescent air and the near flow field becomes quasi-periodic after three wing beats. Therefore, for each CFD case, we select 1000 uniformly distributed points in time over the fourth cycle to fit the model coefficients of the quasi-steady model. For example, for a specified velocity $\boldsymbol{u}_{eg}$, a total of n CFD cases with different wing kinematics are run. Then, a total of $1000n$ data samples of the CFD forces are selected and $1000n$ instantaneous forces of the quasi-steady model are evaluated. The least square error of the force evaluated by the quasi-steady model relative to the CFD reference data is calculated as

$$\begin{aligned}\varepsilon_{ls}(\boldsymbol{u}_{eg}) &= \sum_{i=1}^{n}\sum_{k=1}^{1000}[F^i_{QSM,N}(t_k) - F^i_{CFD,N}(t_k)]^2 \\ &= \sum_{i=1}^{n}\sum_{k=1}^{1000}\left[\sum_{j=1}^{6} I_j(\boldsymbol{u}_{eg})F^i_j(t_k) - F^i_{CFD,N}(t_k)\right]^2, \end{aligned} \tag{4.1}$$

where $F^i_{QSM,N}(t_k)$ is the aerodynamic force normal to the wing surface calculated by (2.9) and (2.21), $F^i_{CFD,N}(t_k)$ is the aerodynamic force normal to the wing surface from the CFD simulation. Then the coefficients parameterizing the quasi-steady model for this velocity $\boldsymbol{u}_{eg}$ can be obtained by minimizing $\varepsilon_{ls}(\boldsymbol{u}_{eg})$, so called the least square method,

$$\begin{aligned} I(\boldsymbol{u}_{eg}) = &\left[\sum_{i=1}^{n}\sum_{k=1}^{1000}\begin{pmatrix} F^i_1(k)F^i_1(k) & \cdots & F^i_6(k)F^i_1(k) \\ \vdots & \ddots & \vdots \\ F^i_1(k)F^i_6(k) & \cdots & F^i_6(k)F^i_6(k)\end{pmatrix}\right]^{-1} \\ &\times\left[\sum_{i=1}^{n}\sum_{k=1}^{1000}\begin{pmatrix} F^i_{CFD,N}(k)F^i_1(k) \\ \vdots \\ F^i_{CFD,N}(k)F^i_6(k)\end{pmatrix}\right]. \end{aligned} \tag{4.2}$$

As can be seen from table 3, 12 different velocities are selected, so 12 sets of $[C_T, C_R, C_D, C_{rd}, A_1, A_2]$ are fitted here. Then, an interpolation method is adopted to predict the coefficients for arbitrary velocity of the insect. We adopt the Kriging surrogate model as the interpolation method which is available as a MATLAB toolbox DACE by Lophaven *et al.* (2002). The procedure is graphically illustrated in figure 5. Twelve distinct velocities as shown in table 3 and the corresponding 12 sets of fitted coefficients $[C_T, C_R, C_D, C_{rd}, A_1, A_2]$ are the inputs and outputs, respectively, to inform the Kriging surrogate model.

After the quasi-steady model coefficients are set, the performance of the model is evaluated on the CFD training data set and the test data set, using the least square error

$$\varepsilon_{ls} = \|Q_{QSM} - Q_{CFD}\|_2^2, \tag{4.3}$$

where Q_{QSM} and Q_{CFD} denote the aerodynamic quantities (such as aerodynamic forces, torques, power, etc.) calculated using the quasi-steady model and the CFD simulation data, respectively.

Figure 6 shows the least square error of the quasi-steady model. It can be seen that the accuracy on the test data set is well consistent with that on the training data set, which

https://doi.org/10.1017/jfm.2021.68 Published online by Cambridge University Press

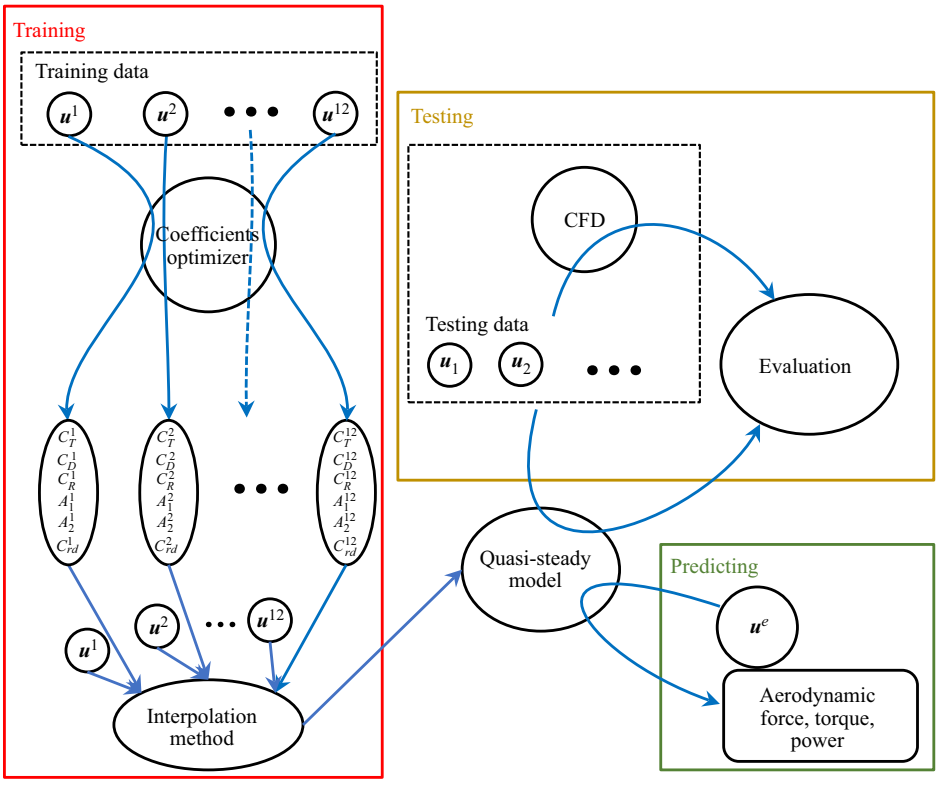


Figure 5. The whole procedure to construct the quasi-steady model for a flapping wing. Coefficients optimizer is formalized by (4.2) which is used to fit the coefficients of selected velocities. The interpolation method is implemented to obtain the coefficients for arbitrary flying velocity to enclose the quasi-steady model for a flapping wing which is realized by a MATLAB toolbox DACE (Lophaven, Nielsen & Søndergaard 2002). Random velocities are selected as testing data to evaluate the accuracy of the quasi-steady model by comparing the simulation results from the quasi-steady model and CFD. Thereafter, the quasi-steady model can be used to predict the aerodynamic force, torque and power of the flapping wings.

is also shown in table 6. Least square error is used to fit the coefficients, but to measure the accuracy of the quasi-steady model in practical applications like stability analysis and controller design, the cycle-averaged aerodynamic force, torque and power consumption are commonly used. Actually, the error of cycle-averaged quantities can be bounded by the least square error

$$\begin{aligned} |\bar{Q}_{QSM} - \bar{Q}_{CFD}| &= \left| \frac{1}{1000} \sum_{i=1}^{1000} (Q^i_{QSM} - Q^i_{CFD}) \right| \\ &\leq \frac{1}{1000} \sum_{i=1}^{1000} |Q^i_{QSM} - Q^i_{CFD}| \\ &\leq \sqrt{\frac{1}{1000} \sum_{i=1}^{1000} |Q^i_{QSM} - Q^i_{CFD}|^2} = \varepsilon_{ls}. \end{aligned} \tag{4.4}$$

https://doi.org/10.1017/jfm.2021.68 Published online by Cambridge University Press

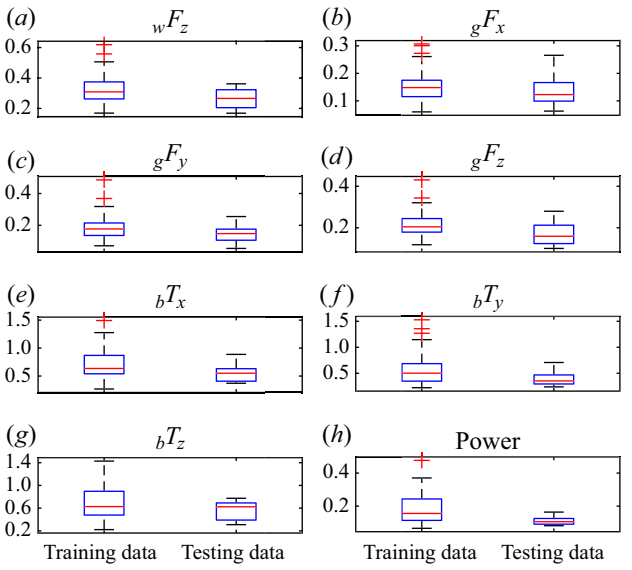


Figure 6. Box plots of the least square error of the quasi-steady model for a flapping wing on both the CFD training data set and test data set on the aerodynamic force normal to the wing surface and its three components in the ground frame (non-dimensionalized by $\rho U_{ref}^2 c_m^2$), three components of the aerodynamic torque in the body frame (non-dimensionalized by $\rho U_{ref}^2 c_m^3$) and the aerodynamic power (non-dimensionalized by $\rho U_{ref}^3 c_m^2$).

Quasi-steady model		$_wF_z$	$_gF_x$	$_gF_y$	$_gF_z$
	Training data	0.32(0.08)	0.15(0.05)	0.18(0.07)	0.21(0.05)
	Test data	0.26(0.06)	0.14(0.05)	0.15(0.05)	0.17(0.05)
		$_bT_x$	$_bT_y$	$_bT_z$	power
	Training data	0.71(0.25)	0.56(0.28)	0.69(0.27)	0.18(0.08)
	Test data	0.55(0.15)	0.39(0.14)	0.58(0.16)	0.11(0.03)
Simplified aerodynamic model			$_gF_x$	$_gF_y$	$_gF_z$
	Training data	—	0.12(0.05)	0.13(0.11)	0.13(0.05)
	Test data	—	0.08(0.04)	0.08(0.03)	0.07(0.03)
		$_bT_x$	$_bT_y$	$_bT_z$	power
	Training data	0.03(0.03)	0.19(0.09)	0.20(0.17)	0.04(0.02)
	Test data	0.08(0.04)	0.08(0.03)	0.07(0.03)	0.02(0.01)

Table 6. Mean values of the least square errors of the forces (non-dimensionalized by $\rho U_{ref}^2 c_m^2$), torques (non-dimensionalized by $\rho U_{ref}^2 c_m^3$) and powers (non-dimensionalized by $\rho U_{ref}^3 c_m^2$) for the quasi-steady model and the simplified aerodynamic model. Values in the parentheses represent the standard deviations.

Figure 7 shows the comparison of cycle-averaged aerodynamic quantities between the prediction of the quasi-steady model and CFD results. It can be seen that all the dots are close to the diagonal solid line which indicates that the predictions of the quasi-steady model approach is close to the CFD results for both the training data set and test data set. This validates the predictive capacity of the quasi-steady model. Thus, the quasi-steady model adequately approximates the aerodynamic mechanisms of flapping wings using a reduced parameter space.

https://doi.org/10.1017/jfm.2021.68 Published online by Cambridge University Press

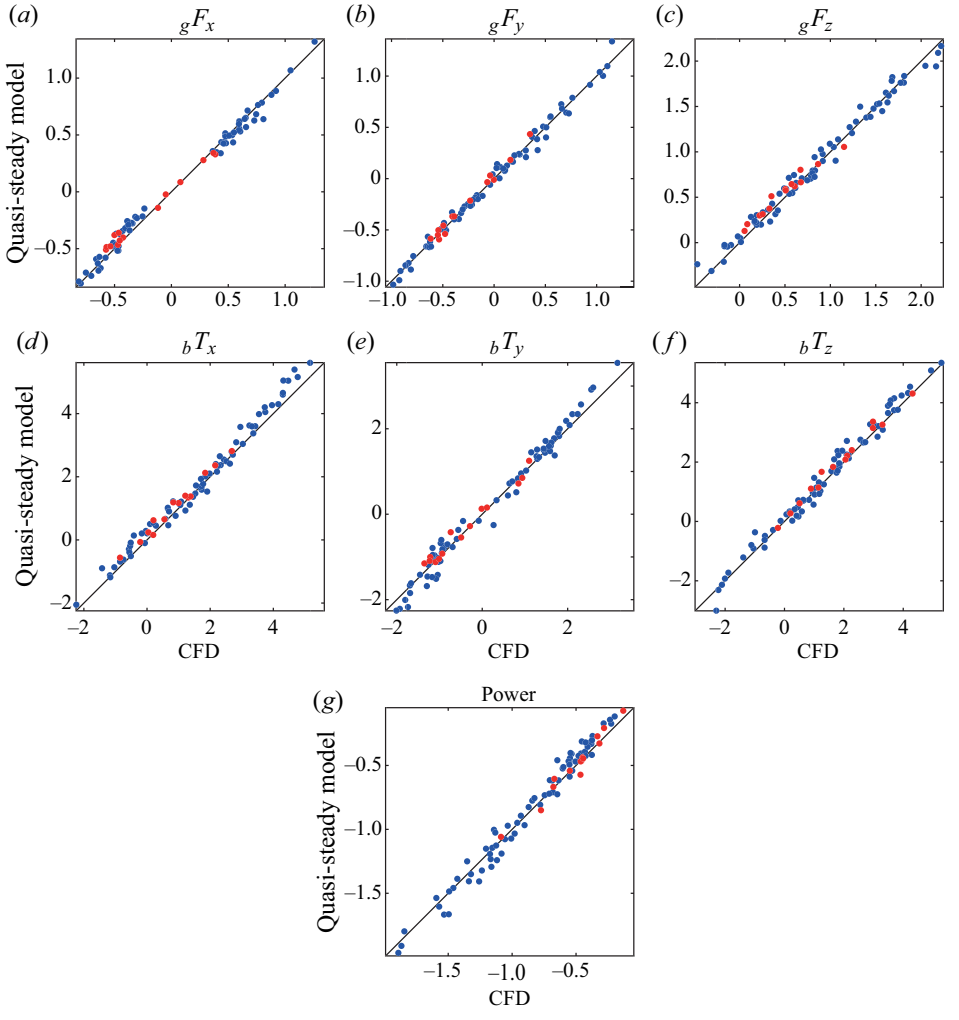


Figure 7. Comparison between the prediction of the quasi-steady model and CFD database for a flapping wing. (*a–c*) Aerodynamic forces in the ground frame, non-dimensionalized by $\rho U_{ref}^2 c_m^2$. (*d–f*) Aerodynamic torques with respect to the centre of body mass of a modelled bumblebee in the body-fixed frame, non-dimensionalized by $\rho U_{ref}^2 c_m^3$. (*g*) Aerodynamic power consumptions, non-dimensionalized by $\rho U_{ref}^3 c_m^2$. Blue: training database. Red: test database. The solid line represents the equality of prediction of the quasi-steady model and CFD results.

Figures 8(*a*) and 8(*b*) show the comparison of lift and drag coefficients between the quasi-steady model and CFD results. The translational lift and drag generated by CFD simulation is obtained by subtracting the rotational circulation force, rotational drag and added mass from the force simulated by the CFD. Figure 8(*c*) shows the comparison of torque coefficients between the quasi-steady model and CFD results. The lift, drag and torque coefficients are defined as

$$C_L = \frac{2Lift}{\int_0^R \rho c v^2 \,\mathrm{d}r}, \quad C_D = \frac{2Drag}{\int_0^R \rho c v^2 \,\mathrm{d}r}, \quad C_M = \frac{2Torque}{\int_0^R \rho c r v^2 \,\mathrm{d}r}. \tag{4.5}$$

https://doi.org/10.1017/jfm.2021.68 Published online by Cambridge University Press

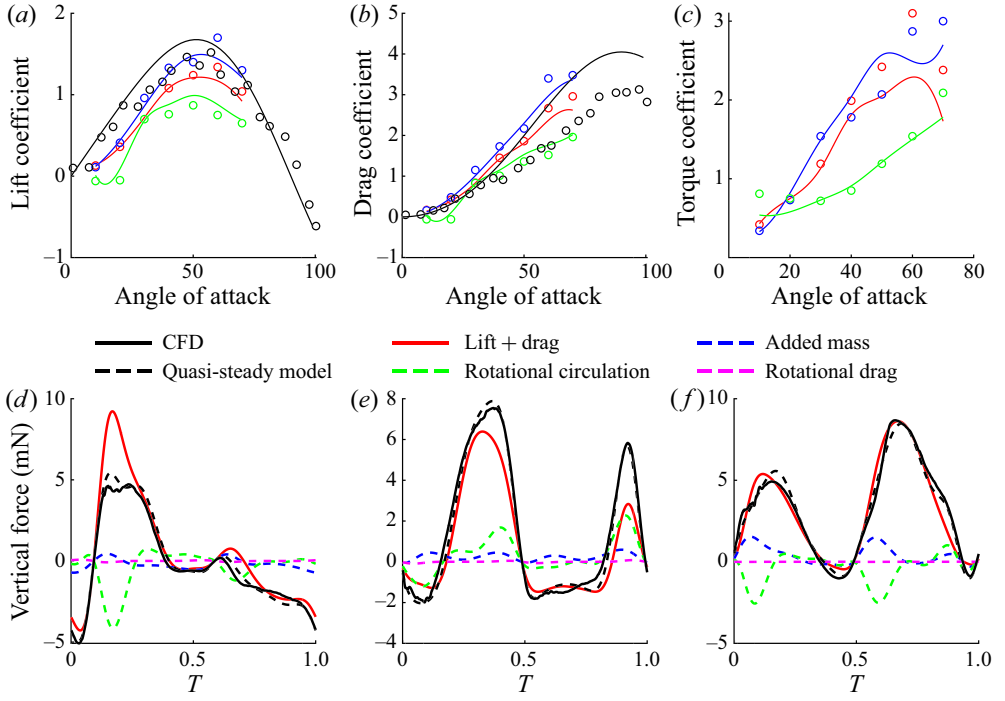


Figure 8. (*a*) Translational lift, (*b*) translational drag and (*c*) torque coefficients for forward $0.4U_{ref}$, rightward $0.4U_{ref}$ and upward $0.4U_{ref}$ (red), forward $0.4U_{ref}$, leftward $0.4U_{ref}$ and upward $0.4U_{ref}$ (blue) and backward $0.4U_{ref}$, rightward $0.4U_{ref}$ and zero vertical speed (green). Line: quasi-steady model. Circle: CFD. The lift coefficient (*a*) and drag coefficient (*b*) for a hovering revolving wing by the present model (black line) and measured by Usherwood & Ellington (2002) (black circles) are also shown for comparison. (*d–f*) Force components of the quasi-steady model in comparison with the CFD results corresponding to the three flying velocities: $(-0.4, 0.4, 0.4)U_{ref}$, $(-0.4, -0.4, 0.4)U_{ref}$ and $(0.4, 0.4, 0)U_{ref}$.

Both lift and drag coefficients of the quasi-steady model agree with CFD results well. When the angle of attack is large, the torque coefficient of the quasi-steady model is generally lower than that of CFD. This may be because of the underestimation of spanwise torque for a high angle of attack. Figures 8(*d*)–8(*f*) show the comparison between the quasi-steady model and CFD for different flight velocities. The translational lift and drag are the dominant contributors to the force generation. The rotational circulation force is also an important component for force generation, which captures the coupling effect between translation motion and rotation motion. The added mass effect plays a minor role in force generation. The contribution to vertical force of rotation drag is very small, partly because the rotation velocity peaks during the stroke reversal where the rotational drag is almost horizontal. The lift and drag coefficients for a hovering revolving wing by the proposed model is also compared with the experimental results (Usherwood & Ellington 2002), as shown in figures 8(*a*) and 8(*b*). The lift coefficient by the proposed model is almost identical to the experimental results and the proposed model overestimates the drag coefficient for an angle of attack larger than 40 degrees. This overestimation may be because the drag coefficient by the proposed model is fitted from a flapping wing rather than a revolving wing.

https://doi.org/10.1017/jfm.2021.68 Published online by Cambridge University Press

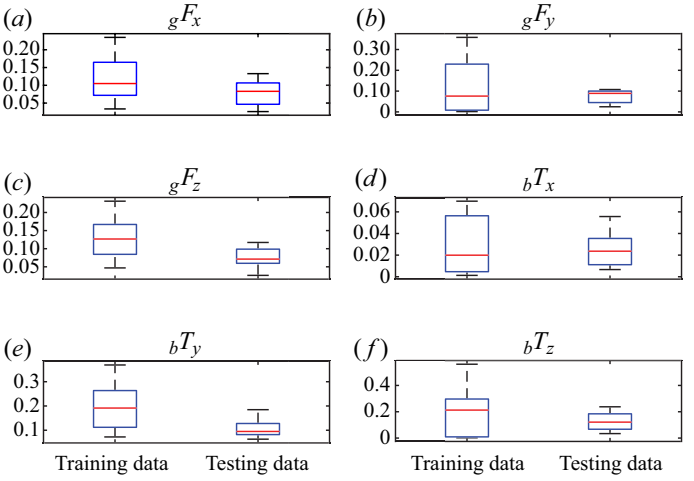


Figure 9. Box plots of the least square error of a simplified aerodynamic model for the moving body on both the CFD training data set and testing data set. (*a–c*) The three components of aerodynamic force in the ground frame (non-dimensionalized by $\rho U_{ref}^2 c_m^2$). (*d–f*) The three components of the aerodynamic torque with respect to the centre of body mass in the body frame (non-dimensionalized by $\rho U_{ref}^2 c_m^3$).

$C_{bd,L}$	$C_{bd,D}(0)$	$C_{bd,D}\,(\pi/2)$	x_p (mm)	z_p (mm)
0.0701	0.0465	0.1604	−0.3118	−0.0081

Table 7. Fitted coefficients of the simplified aerodynamic model for a moving body of a bumblebee.

4.2. *Simplified aerodynamic model for a moving body*

As explained in § 2.3, five constant coefficients $[C_{bd,L}, C_{bd,D}(0), C_{bd,D}(\pi/2), x_p, z_p]$ parameterizing the simplified aerodynamic model are fitted by minimizing the least square error for the CFD training data set. The results for a bumblebee are listed in table 7. Comparing the least square error of the training and the test data sets, it can be seen that the simplified aerodynamic model performs adequately; see figure 9. Compared with figure 6, the least square error in figure 9 is smaller, which demonstrates that the simplified aerodynamic model for the body is accurate enough to predict the aerodynamic force and torque of the moving body, which is also shown in table 6.

Figure 10 shows the comparison of the cycle-averaged aerodynamic quantities between the simplified aerodynamic model and CFD results for the moving body. The simplified aerodynamic model performs consistently on both training data set and test data set.

4.3. *Aerodynamic performance of the CDAM of a bumblebee*

Sections 2, 4.1 and 4.2 discussed and validated the quasi-steady model for flapping wings and the simplified aerodynamic model for a moving body separately. Here, we combine them in one model, i.e. the CDAM. Figure 11 shows the comparison between the predictions using CDAM and the results of CFD simulation. The predictions by the CDAM are well consistent with the CFD results.

https://doi.org/10.1017/jfm.2021.68 Published online by Cambridge University Press

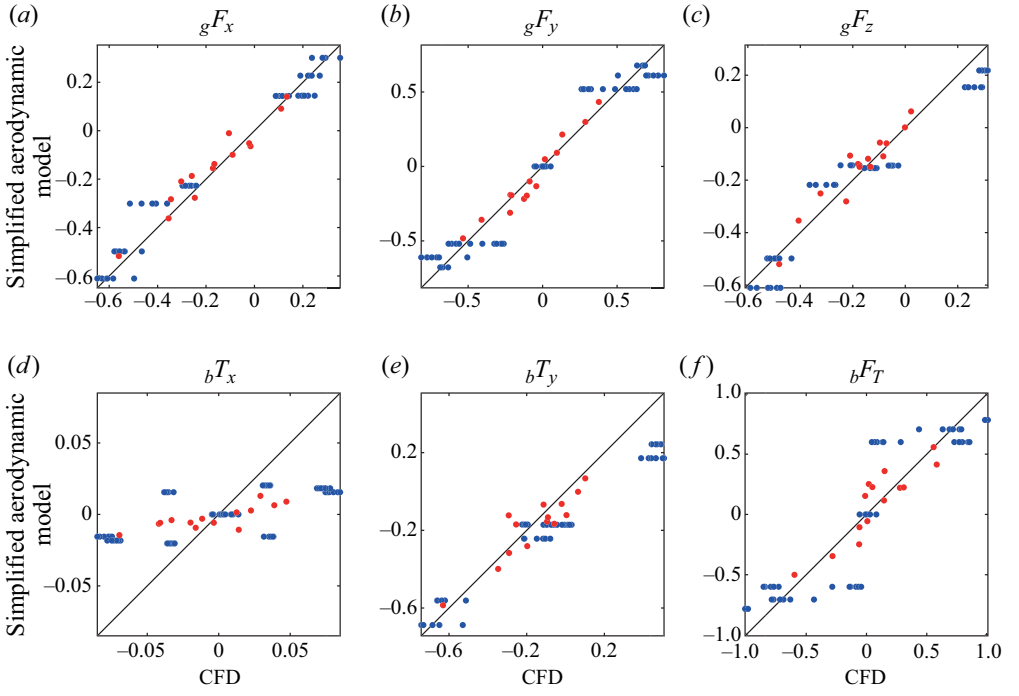


Figure 10. Comparison between the prediction of the simplified aerodynamic model and CFD database for a moving body. (*a–c*) Aerodynamic forces in the ground frame, non-dimensionalized by $\rho U_{ref}^2 c_m^2$. (*d–f*) Aerodynamic torques with respect to the centre of body mass of a modelled bumblebee in the body-fixed frame, non-dimensionalized by $\rho U_{ref}^2 c_m^3$. Blue: training database. Red: test database. The solid line represents the equality of prediction of the simplified aerodynamic model and CFD results.

4.4. *Discussion on the dependence of coefficients on forward flight conditions from the standpoint of fluid dynamics*

The quasi-steady approach only uses the instantaneous motion of the flapping wing to predict the aerodynamic loads, while the real fluid motion around the wing has time memory. Taking hovering as an example, as shown in figure 12, compared with the first stroke cycle, the vertical force of the following stroke cycles decreases by about 15 %. This reduction is due to the existence of downwash as shown in figure 13.

Although there exist reliable downwash models for hovering flight (Oh *et al.* 2020), they are unlikely to generalize to arbitrary flight conditions. As shown in figure 12, the wake is almost fully developed at the second stroke cycle. The variation of the peak value during a downstroke is negative for hovering and slow forward speed 1 m s^{-1} and positive for relatively fast forward speeds 2, 3, 4 and 5 m s^{-1}. The variation reaches maximum for medium forward velocity 2 and 3 m s^{-1}.

In comparison with the flapping in quiescent air during the first stroke cycle, the surrounding flow (during the second stroke cycle) induced by the previous cycle varies with the flight speed. Figure 13 shows the flow field around the mid-downstroke during the first and second stroke cycles. It can be seen that before the mid-downstroke for hovering, there exists a large area of flow with downward velocity, called downwash. When the wing encounters this downwash, the effective angle of attack decreases which causes the reduction of lift. In this study, the effect of downwash is included into the

https://doi.org/10.1017/jfm.2021.68 Published online by Cambridge University Press

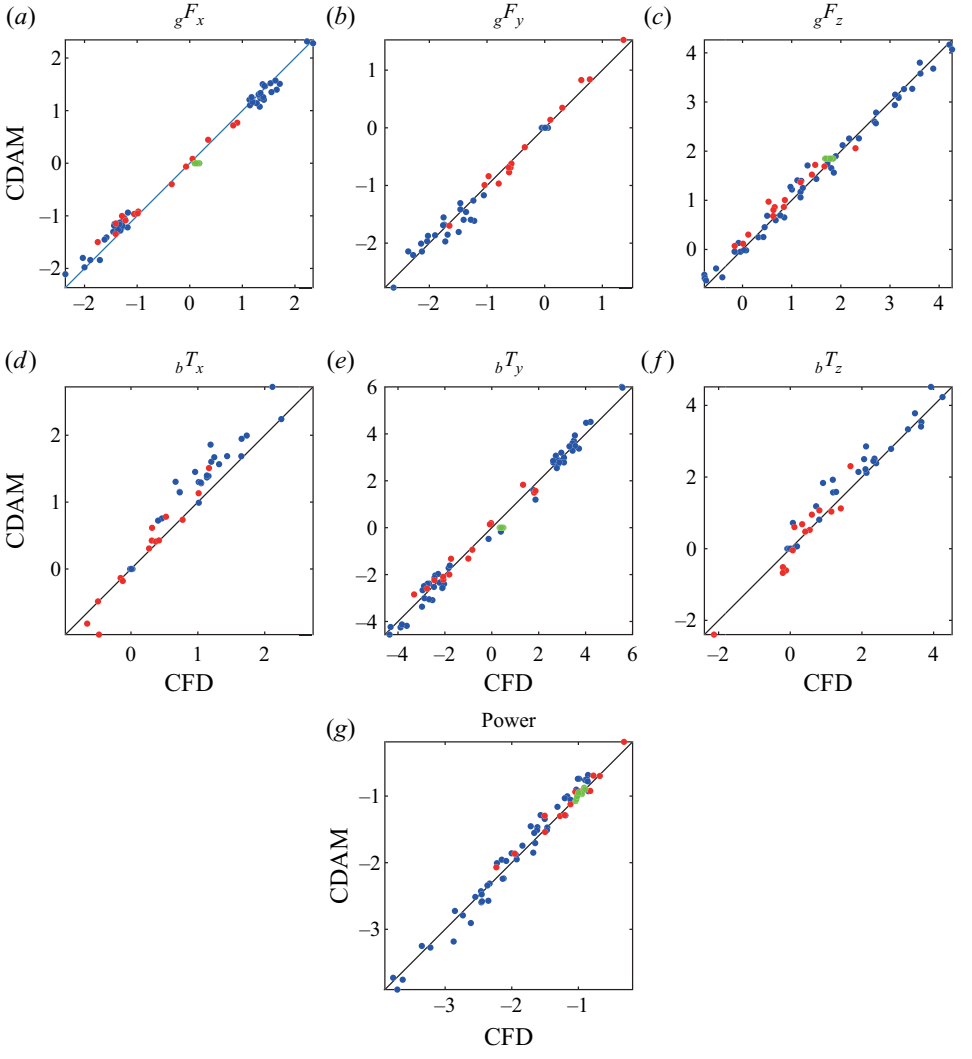


Figure 11. Comparison between the prediction of the CDAM and CFD database for a bumblebee. (*a–c*) Aerodynamic forces in the ground frame, non-dimensionalized by $\rho U_{ref}^2 c_m^2$. (*d–f*) Aerodynamic torques with respect to the centre of body mass of a modelled bumblebee in the body-fixed frame, non-dimensionalized by $\rho U_{ref}^2 c_m^3$. (*g*) Aerodynamic power consumptions, non-dimensionalized by $\rho U_{ref}^3 c_m^2$. Blue: training database. Red: test database. Green: trim states listed in table 8. The solid line represents the equality of prediction of the quasi-steady model and CFD results.

fitted coefficients. Conversely, for a forward speed of 3 m s^{-1}, there exists an area of flow with upward velocity, we call it upwash. During the downstroke, the wing encounters this upwash, the effective angle of attack increases which causes the rise of lift. For a large forward speed of 5 m s^{-1}, there also exists an area of flow with upward velocity, but it is weaker than that for a 3 m s^{-1} forward speed, so its contribution to lift enhancement is small. To elucidate how the downwash and upwash are generated and how they interact with the flapping wing, we illustrate the vortex structure around the flying bumblebee; see figure 14. For all the three forward speeds, there is a vortex tube connecting to the wing tip

https://doi.org/10.1017/jfm.2021.68 Published online by Cambridge University Press

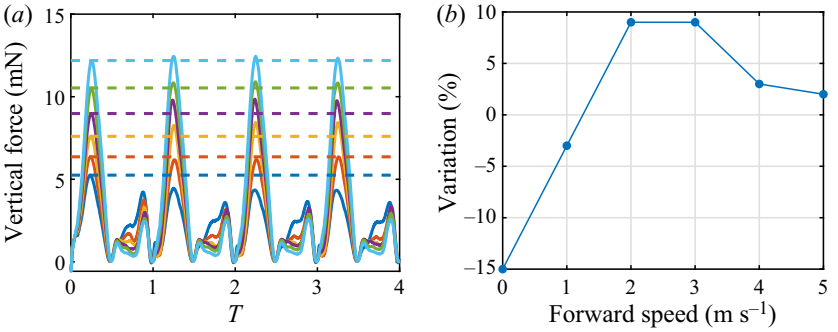


Figure 12. (*a*) Time course of the vertical force with the corresponding coloured dashed lines representing the peak value of the downstroke in the first stroke cycle from bottom up: hovering (0 m s^{-1}) and forward speed 1, 2, 3, 4 and 5 m s^{-1}. (*b*) Difference of the peak value of the vertical force in the downstroke between the first and second stroke cycle.

behind the wing during upstroke which originates from the detached trailing edge vortex; see figure 14(*a–c*). The fluid flows downward through the area bounded by the vortex tube and the wing. Outside this area, the fluid flows upward. Such fluid motion is maintained by the vortex tube in the following downstroke but its interaction with the flapping wing varies with forward speed. For hovering, the downwash locates by the side of the body. This downwash interacts with the flapping wing, resulting in a reduction of force; see figure 14(*d*). For the forward speed 3 m s^{-1}, the vortex tube moves behind the bumblebee and the upwash moves to the side of the body and interacts with the flapping wing resulting in increment of force; see figure 14(*e*). For the forward speed 5 m s^{-1}, the vortex tube moves further behind the bumblebee and both the areas of downwash and upwash move behind the bumblebee, so there are almost no interactions between the downwash and/or upwash and flapping wing; see figure 14(*f*).

Quasi-steady models predict the aerodynamic loads only based on the instantaneous wing motion which cannot include the complex interaction of the wing and the pre-developed flows for a variety of flight speeds. By collecting a large database of CFD simulations, the coefficients parameterizing the quasi-steady model can thereby be informed to include such speed-varying flow effects. The relationship between the trained coefficients and forward velocities is illustrated by figure 15. The trained coefficients present a strong dependency on the forward velocity-related unsteady aerodynamics. Thus, the model is well trained to capture the forward-velocity-dependent unsteady aerodynamic effects compared with previous studies. For hovering, the trained translational lift coefficient C_T is well consistent with that of previous work (Berman & Wang 2007). The trained translational drag coefficient C_D is comparatively larger than that of a previous study (Berman & Wang 2007), which originates from a translational wing (Usherwood & Ellington 2002), as shown in figure 8(*b*). A theoretical formula for the translational drag coefficient has been provided by Wang *et al.* (2016), that is, $C_D = 2\pi\mathcal{R}/(\sqrt{\mathcal{R}^2+4}+2)$, which is equal to 3.75 for the bumblebee in this study with aspect ratio $\mathcal{R} = 3.71$ and is well consistent with the trained C_D equal to 4.05. The trained rotational lift coefficient C_R is comparatively larger than that with the value π of previous studies (Ellington & Lighthill 1984; Berman & Wang 2007), which is theoretically derived for inviscid flows. It has been found that the theoretical C_R may cause poor predictions and needs to be modified to achieve good agreements (Wang *et al.* 2016; Bluman & Kang 2017), which may explain the difference between the trained rotational lift coefficient and the

https://doi.org/10.1017/jfm.2021.68 Published online by Cambridge University Press

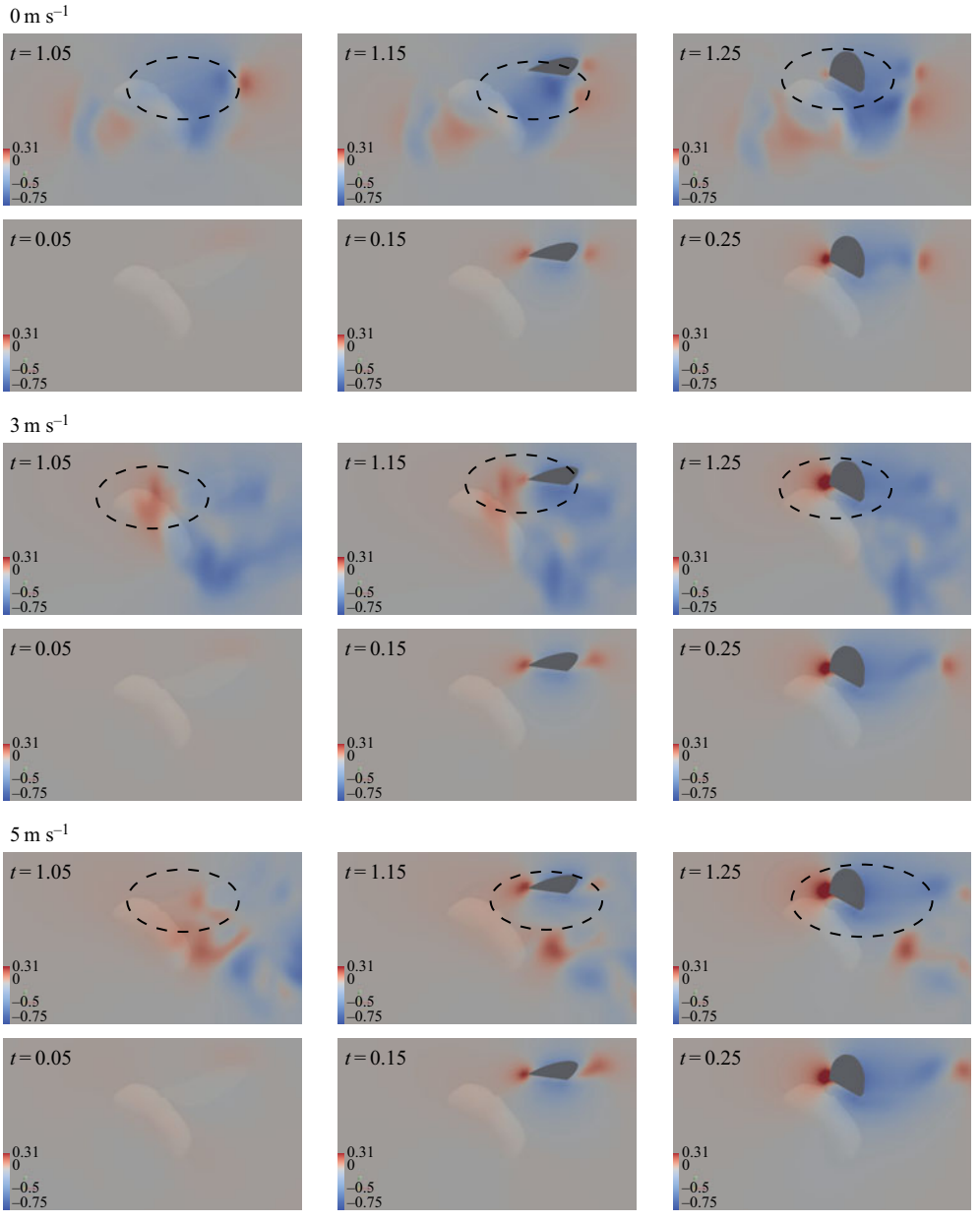


Figure 13. The vertical velocity non-dimensionalized by U_{ref} of the air flow on the vertical cut plane $2c_m$ away from the sagittal plane of the bumblebee for hovering, forward speed 3 and 5 m s^{-1} in the first and second stroke cycle. Red indicates the air flowing upwards and blue indicates the air flowing downwards.

theoretical one. The trained C_{rd} and A_1 also deviate from those of a previous study, which may be because the rotational drag and added mass contribute insignificantly to the force production, as shown in figures 8(*d*)–8(*f*), and variation in the magnitudes of C_{rd} and A_1 do not alter the force production. The feature of downwash-to-upwash transition is also well captured in terms of the rapid increase in C_T and the convex-like variation in C_R, C_D, C_{rd}, A_1 and A_2. In conclusion, the CFD-informed method based on the solutions

https://doi.org/10.1017/jfm.2021.68 Published online by Cambridge University Press

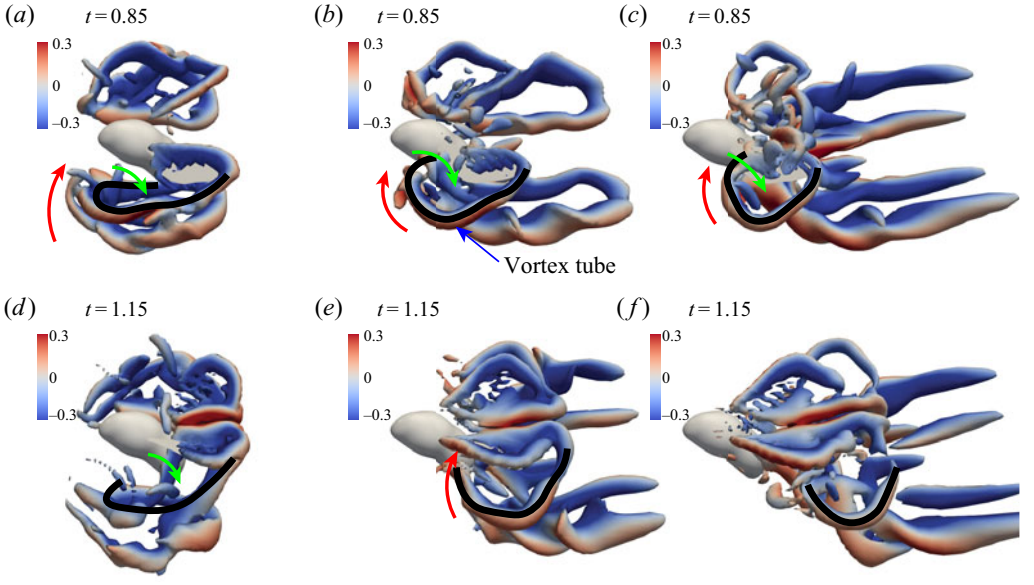


Figure 14. Vortical structures around a flying bumblebee (isosurface with $Q = 0.1$, coloured by vertical velocity non-dimensionalized by U_{ref}). (*a*,*d*) Hovering; (*b*,*e*) forward speed 3 m s^{-1}; (*c*,*f*) forward speed 5 m s^{-1}. Red arrows: upward flow; green arrows: downward flow. Black curve: vortex tube.

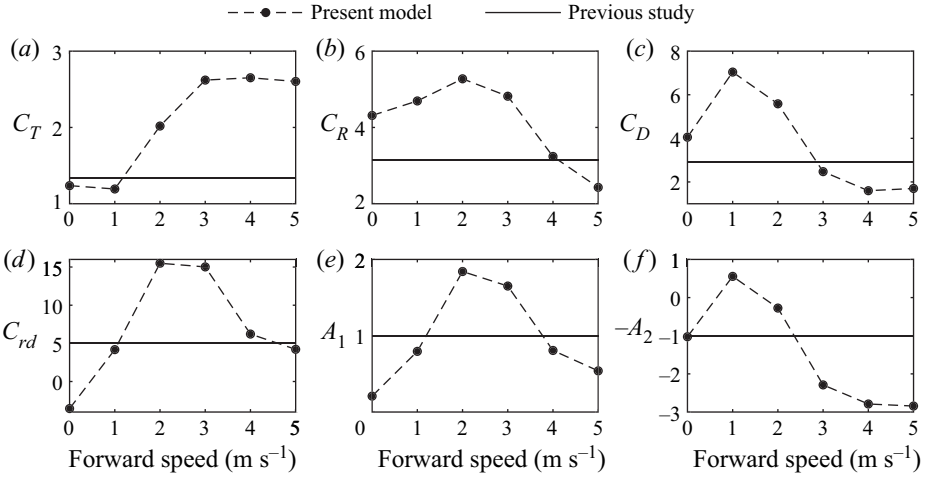


Figure 15. Variation of trained aerodynamic coefficients with forward velocity. C_T, C_R, C_D (by Usherwood & Ellington 2002; Berman & Wang 2007), C_{rd}, A_1 and A_2 (by Whitney & Wood 2010) from a previous study are shown for comparison.

to the Navier–Stokes equations can assure the fundamental unsteady aerodynamics (fluid physics) associated with flapping flights in arbitrary flight velocities, which ensures the CFD-informed quasi-steady approach is capable of a fast and precise prediction of flapping aerodynamics. If the flight speed is arbitrary, the unsteady aerodynamic effects can be more complicated. With the aid of the CFD data-driven method, despite the complexity of the air flow, the quasi-steady approach is applicable to arbitrary flight speed.

https://doi.org/10.1017/jfm.2021.68 Published online by Cambridge University Press

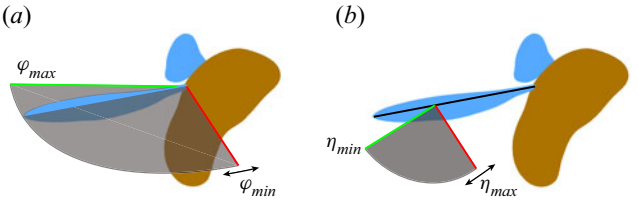


Figure 16. Sketch of the extrema of wing kinematics. (*a*) Positional angle. (*b*) Feathering angle.

5. Trim state of modelled bumblebee in forward flight

The CDAM is demonstrated to precisely predict the aerodynamic force, torque and power for a flying bumblebee with a vast range of velocity and various wing kinematics. Now, we further demonstrate the predictive capacity of CDAM by finding the trim state of a bumblebee in forward flight. In forward flight, the body posture, stroke plane and wing kinematics differ from those in hovering flight. If a bumblebee flies forward at a constant speed, its equilibrium state has to satisfy three conditions (so called trim conditions): cycle-averaged forward/backward aerodynamic force equals zero; cycle-averaged vertical aerodynamic force equals the weight of the bumblebee; cycle-averaged aerodynamic pitching moment equals zero. Here, a genetic optimization algorithm based on the derandomized evolution strategy with covariance matrix adaptation is used to find the trim state (Hansen, Müller & Koumoutsakos 2003; Hansen & Kern 2004). The cost function is defined as

$$c = {}_g\bar{F}_x^2 + ({}_g\bar{F}_z - W)^2 + {}_b\bar{T}_y^2, \tag{5.1}$$

where ${}_g\bar{F}_x$ is the cycle-averaged forward/backward aerodynamic force, ${}_g\bar{F}_z$ is the cycle-averaged vertical aerodynamic force, W is the weight of the bumblebee, ${}_b\bar{T}_y$ is the cycle-averaged aerodynamic pitching moment.

Keeping the body angle, the stroke plane angle and the forward velocity constant, we tune the wingbeat frequency, the positional angle amplitude and mean value, and the feathering amplitude and mean value. The minimal positional angle (φ_{min}) is varied to control the flapping amplitude and mean value, while the maximal positional angle (φ_{max}) remains constant during the optimization. The maximal feathering angle (η_{max}) is varied to control the feathering amplitude and mean value, while the minimal feathering angle (η_{min}) remains constant during the optimization. This is illustrated in figure 16. The genetic algorithm is used to tune the three input variables (f, φ_{min} and η_{max}) to minimize the cost function. If the trim condition is reached, the cost function becomes zero. The initial value of the frequency is 136 Hz, the initial flapping angle amplitude is 137° and the initial feathering angle amplitude is 125°. According to the measurements on the bumblebees done by Dudley & Ellington (1990*a*), we set the upper bound in the genetic optimization algorithm (Hansen *et al.* 2003; Hansen & Kern 2004) to [175 Hz, 140°, 140°] and the lower bound to [120 Hz, 90°, 100°]. We set initial population with size 50 randomly sampled within the lower bound and upper bound. It would be prohibitively time consuming to minimize the cost function (5.1) using CFD simulation directly to calculate the aerodynamic forces and torques. Instead, we use CDAM. It took about 1000 evaluations (∼10 min) to complete the optimization. Here, we focus on the flight with forward speed 1.005 m s^{-1}. The trim states found are listed in table 8. To check the accuracy of the trim states found by the CDAM, the predictions of both CDAM and CFD are plotted in figure 11(*a*,*c*,*e*,*g*). The agreement is satisfactory.

https://doi.org/10.1017/jfm.2021.68 Published online by Cambridge University Press

No.	Body angle (deg.)	Stroke plane angle (deg.)	Frequency (Hz)	Flapping amplitude (deg.)	Feathering amplitude (deg.)
1	45	0	123	135	114
2	45	5	127	132	121
3	45	10	132	130	129
4	40	0	130	127	114
5	40	5	134	124	122
6	40	10	140	122	129
7	35	0	137	120	115
8	35	5	142	117	122
9	35	10	149	114	130
10	25	0	153	106	116
11	15	0	171	94	118

Table 8. Trim states of a flying bumblebee with forward speed 1.005 m s^{-1}.

The solution for the trim conditions is the intersection of three isosurfaces, i.e. ${}_g\bar{F}_x = 0$, ${}_g\bar{F}_z = W$ and ${}_b\bar{T}_y = 0$. Here, we plot the three isosurfaces for case 6 listed in table 8 with the body angle and the stroke plane angle similar to those measured by Dudley & Ellington (1990*a*,*b*); see figure 17. For the isosurface ${}_g\bar{F}_x = 0$, the feathering amplitude is almost constant, so the forward/backward force ${}_g\bar{F}_x$ is sensitive to the feathering amplitude and insensitive to the flapping amplitude and frequency. From the isosurface ${}_g\bar{F}_z = W$, it can be concluded that the vertical force ${}_g\bar{F}_z$ is weakly sensitive to feathering amplitude. From the isosurface ${}_b\bar{T}_y = 0$, it can be concluded that the pitch torque ${}_b\bar{T}_y$ is not sensitive to the flapping frequency. To balance the pitch torque, the feathering amplitude has to be increased for smaller flapping amplitudes, and vice versa. There is only one point of intersection of the three isosurfaces, hence, there is only one solution to the trim conditions, if the body and the stroke plane angles are prescribed.

More generally, from table 8, it can be seen that, for a specific forward speed, the trim state is not unique, so the bumblebee may easily reach equilibrium from an arbitrary condition. Let us consider the mass-specific aerodynamic power consumption

$$P^* = \frac{power}{m_t}. \tag{5.2}$$

We find that there is an essentially linear relationship between the body angle, the stroke plane angle and the mass-specific aerodynamic power consumption, as shown in figure 18, determined by linear regression

$$P^* = 48.2138 + 0.1997(\beta - 4.5986\theta_{SP}), \tag{5.3}$$

with correlation coefficient $R^2 = 0.9819$. Dudley & Ellington (1990*a*,*b*) measured the body posture and wing kinematics of a forward flying bumblebee and estimated the power consumption. We extracted the body angle, the stroke plane angle and mean mass-specific mechanical power of three individual bumblebees from the above references and added these points on the diagram in figure 18. Although the size, mass and wing kinematics of the bumblebees measured by Dudley & Ellington (1990*a*,*b*) and the modelled bumblebee in this study are different, there is also a linear relationship between the mass-specific aerodynamic power and body angle and stroke plane angle. The power consumption of the

https://doi.org/10.1017/jfm.2021.68 Published online by Cambridge University Press

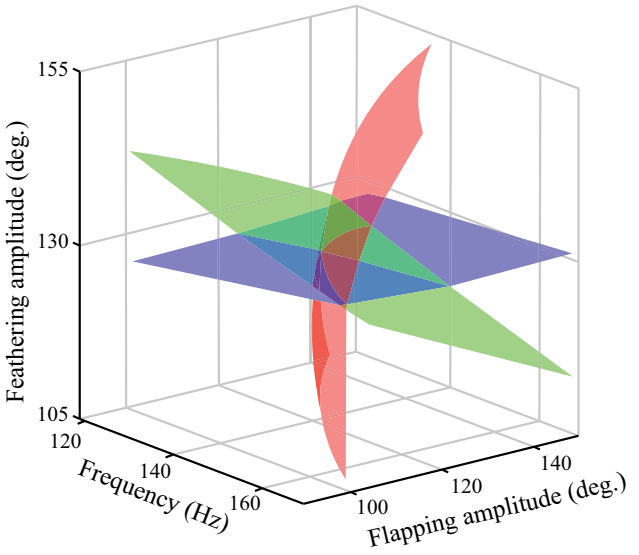


Figure 17. Isosurface ${}_g\bar{F}_x = 0$ (blue), ${}_g\bar{F}_z = W$ (red) and ${}_b\bar{T}_y = 0$ (green) in the space spanned by the feathering amplitude, frequency and flapping amplitude.

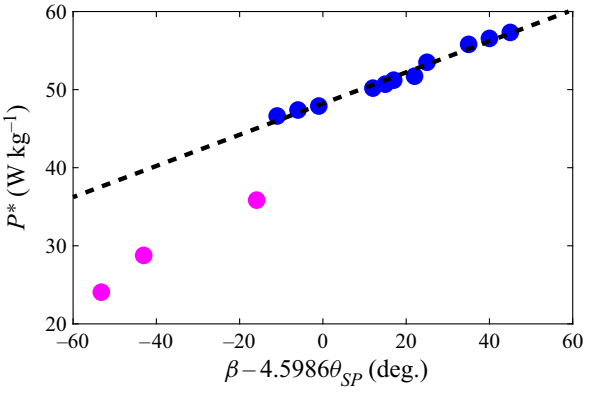


Figure 18. The linear relationship between body angle, stroke plane angle and mass-specific aerodynamic power consumption. Black line: curve of (5.3). Blue dots: trim states in table 8. Wine red dots: cases extracted from Dudley & Ellington (1990*a*,*b*).

three bumblebees on average is smaller than those shown in table 8. This may suggest that bumblebees prefer trim states with minimal power consumption. Combes *et al.* (2020) studied the effect of stroke amplitude and flapping frequency on the energy cost and inferred that when carrying light loads, stability and/or maneuverability can be improved by increasing the flapping frequency which sacrifices energetic efficiency. In this study, however, for an unloaded bumblebee, power efficiency can be improved for higher flapping frequency by appropriately orienting the attitude of the insect (body angle and stroke plane angle). According to (5.3), bumblebees tend to decrease the body angle and increase the stroke plane angle to decrease the power consumption, under physiological and force generation constrains. For example, the frequency increases with the reduction of the body angle, but the bumblebee cannot increase the frequency indefinitely. We conclude that CDAM can be reliably applied to find trim states in forward flight.

https://doi.org/10.1017/jfm.2021.68 Published online by Cambridge University Press

6. Proportional-derivative controller design for hovering flight using CDAM

Earlier studies of the correlation between the wing kinematics and production of aerodynamic forces and torques (Hedrick & Daniel 2006; Dickinson & Muijres 2016) have enabled the development of insect-inspired flight controllers (Fei *et al.* 2019*b*; Yao & Yeo 2019; Zhang *et al.* 2019). Zhang *et al.* (2019) performed costly CFD simulations to find appropriate control parameters by trial and error. Yao & Yeo (2019) used a simplified aerodynamic model to derive the control parameters. However, when applied in CFD simulations, the parameters needed further adjustment.

Let us evaluate the predictive capability of CDAM from the standpoint of controller design. The CDAM can reasonably predict the aerodynamic loads on the flying bumblebee with a variety of velocities and wing kinematics which makes it suitable for control purposes. We derive a PD controller that effectively enforces longitudinal stability of the hovering bumblebee model. This methodology is applicable in forward flight. Here we apply it on the control to recover from a perturbed state (with slight forward, upward velocity and nose down pitch velocity) to hovering. The control model accounts for the sensorimotor latency. The control parameters are optimized by solving a dynamical system that encapsulates stability derivatives evaluated using CDAM. This significantly reduces the computation time compared with the trial and error method using CFD simulation. In addition, the optimized controller can be directly applied in CFD simulations because CDAM is consistent with CFD by construction.

The flight dynamics of insects is governed by rather tedious differential equations (Sun, Wang & Xiong 2007), if the time-accurate dynamics of flapping wings is included. However, bumblebees are heavy enough and their flapping frequency is large enough so that the fluctuation of inertial forces and torques during one period of wing beat does not influence the body dynamics on the time scale of about 10 wing beats representative of the recovery time of bumblebees after perturbation by strong wind gusts (Jakobi *et al.* 2018). In this section all the quantities are expressed in non-dimensional form. Length, velocity, time, force, torque, mass, moment of inertia are non-dimensionalized by c_m, U_{ref}, U_{ref}/c_m, $\rho c_m^2 U_{ref}^2$, $\rho c_m^3 U_{ref}^2$, ρc_m^3, ρc_m^5, respectively. We therefore consider the cycle-averaged motion of the bumblebee as a solid body,

$$\left.\begin{aligned} m_{tg}\dot{\bar{\boldsymbol{v}}} &= {}_g\bar{\boldsymbol{F}}_{aero} + m_{tg}\boldsymbol{g}, \\ {}_bI_b\dot{\bar{\boldsymbol{\omega}}} &= {}_b\bar{\boldsymbol{M}}_{aero}, \end{aligned}\right\} \tag{6.1}$$

where ${}_g\bar{\boldsymbol{v}}$ is the centre of mass velocity in the ground frame of reference and ${}_b\bar{\boldsymbol{\omega}}$ is the angular velocity of the body in its reference frame, dots denote time derivatives, $m_t = m_b + 2m_w$ is the total mass of the bumblebee and ${}_bI$ is its moment of inertia. For the purpose of longitudinal control with small perturbation near hovering, (6.1) further simplify as

$$\begin{pmatrix} {}_g\ddot{x} \\ {}_g\ddot{z} \\ \ddot{\beta} \end{pmatrix} = \begin{pmatrix} {}_g\tilde{F}_x \\ {}_g\tilde{F}_z - g \\ {}_b\tilde{M}_\beta \end{pmatrix}, \tag{6.2}$$

where ${}_g\tilde{F}_x = {}_g\bar{F}_{aero,x}/m_t$, ${}_g\tilde{F}_z = {}_g\bar{F}_{aero,z}/m_t$ and ${}_b\tilde{M}_\beta = {}_b\bar{M}_{aero,y}/{}_bI_{yy}$ are the cycle-averaged aerodynamic forces divided by the mass $m_t = 3.92 \times 10^{-4}$ kg and the aerodynamic torque divided by the moment of inertia ${}_bI_{yy} = 7.49 \times 10^{-9}$ kg m^2, respectively. As discussed in §§ 2 and 4, the cycle-averaged aerodynamic forces and torques can be accurately predicted by CDAM and they depend on the motion of the flying

https://doi.org/10.1017/jfm.2021.68 Published online by Cambridge University Press

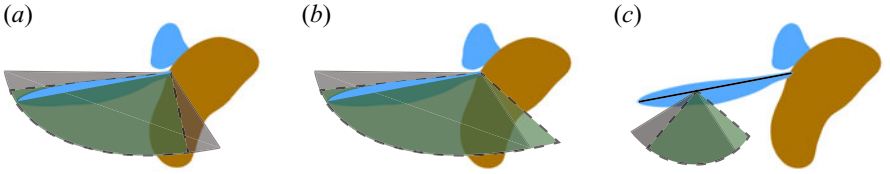


Figure 19. Variation of wing kinematics: (*a*) positional angle amplitude $\Delta\Phi$, (*b*) mean positional angle $\Delta\bar{\varphi}$ and (*c*) mean feathering angle $\Delta\bar{\eta}$.

bumblebee and its wing kinematics. The wing motion should be controlled to maintain the hovering state. Here, we choose to vary the positional angle amplitude $\Delta\Phi$, the mean positional angle $\Delta\bar{\varphi}$ and the mean feathering angle $\Delta\bar{\eta}$ as control inputs; see figure 19. Hence, the quantities ${}_g\tilde{F}_x$, ${}_g\tilde{F}_z$ and ${}_b M_\beta$ are treated as functions of six state variables,

$$\left.\begin{aligned} {}_g\tilde{F}_x &= {}_g\tilde{F}_x({}_g\dot{x},\, {}_g\dot{z},\, \dot{\beta},\, \Delta\Phi,\, \Delta\bar{\varphi},\, \Delta\bar{\eta}),\\ {}_g\tilde{F}_z &= {}_g\tilde{F}_z({}_g\dot{x},\, {}_g\dot{z},\, \dot{\beta},\, \Delta\Phi,\, \Delta\bar{\varphi},\, \Delta\bar{\eta}),\\ {}_b\tilde{M}_\beta &= {}_b\tilde{M}_\beta({}_g\dot{x},\, {}_g\dot{z},\, \dot{\beta},\, \Delta\Phi,\, \Delta\bar{\varphi},\, \Delta\bar{\eta}). \end{aligned}\right\} \tag{6.3}$$

For hovering, $({}_g\tilde{F}_x,\, {}_g\tilde{F}_z,\, {}_b\tilde{M}_\beta)' = (0,\, g,\, 0)'$. Considering small perturbation approximation around hovering, (6.3) can be approximated by the first order of its Taylor series expansion which, after substitution into (6.2), yields the governing dynamic equation near hovering,

$$\begin{pmatrix} {}_g\ddot{x} \\ {}_g\ddot{z} \\ \ddot{\beta} \end{pmatrix} = D \begin{pmatrix} {}_g\dot{x} \\ {}_g\dot{z} \\ \dot{\beta} \end{pmatrix} + W \begin{pmatrix} \Delta\Phi \\ \Delta\bar{\varphi} \\ \Delta\bar{\eta} \end{pmatrix}, \tag{6.4}$$

where D is the damping matrix and W is the effect matrix describing the effect of wing kinematics on the acceleration of the bumblebee,

$$D = \left.\begin{pmatrix} \dfrac{\partial\, {}_g\tilde{F}_x}{\partial\, {}_g\dot{x}} & \dfrac{\partial\, {}_g\tilde{F}_x}{\partial\, {}_g\dot{z}} & \dfrac{\partial\, {}_g\tilde{F}_x}{\partial\dot{\beta}} \\ \dfrac{\partial\, {}_g\tilde{F}_z}{\partial\, {}_g\dot{x}} & \dfrac{\partial\, {}_g\tilde{F}_z}{\partial\, {}_g\dot{z}} & \dfrac{\partial\, {}_g\tilde{F}_z}{\partial\dot{\beta}} \\ \dfrac{\partial\, {}_b\tilde{M}_\beta}{\partial\, {}_g\dot{x}} & \dfrac{\partial\, {}_b\tilde{M}_\beta}{\partial\, {}_g\dot{z}} & \dfrac{\partial\, {}_b\tilde{M}_\beta}{\partial\dot{\beta}} \end{pmatrix}\right|_0, \quad W = \left.\begin{pmatrix} \dfrac{\partial\, {}_g\tilde{F}_x}{\partial\Delta\Phi} & \dfrac{\partial\, {}_g\tilde{F}_x}{\partial\Delta\bar{\varphi}} & \dfrac{\partial\, {}_g\tilde{F}_x}{\partial\Delta\bar{\eta}} \\ \dfrac{\partial\, {}_g\tilde{F}_z}{\partial\Delta\Phi} & \dfrac{\partial\, {}_g\tilde{F}_z}{\partial\Delta\bar{\varphi}} & \dfrac{\partial\, {}_g\tilde{F}_z}{\partial\Delta\bar{\eta}} \\ \dfrac{\partial\, {}_b\tilde{M}_\beta}{\partial\Delta\Phi} & \dfrac{\partial\, {}_b\tilde{M}_\beta}{\partial\Delta\bar{\varphi}} & \dfrac{\partial\, {}_b\tilde{M}_\beta}{\partial\Delta\bar{\eta}} \end{pmatrix}\right|_0. \tag{6.5}$$

Hedrick, Cheng & Deng (2009) in a study of the rotational damping of a hummingbird emphasized the importance of flapping counter torque (FCT). More generally, the damping effects exist in all the six directions (forward/backward, vertical, lateral, yaw, pitch and roll) which are the diagonal elements of the damping matrix. In addition, the off-diagonal elements in D can be large as the motions in all directions are coupled. Cheng *et al.* (2010) studied fast turning maneuvers of fruit fly and pointed out that the passive aerodynamic damping due to FCT can account for a large part of the deceleration during saccades. Values of D and W can be directly obtained using CDAM with a finite difference method, for example, $\partial\, {}_g\tilde{F}_x/\partial\, {}_g\dot{x} \approx ({}_g\tilde{F}_x(\delta\, {}_g\dot{x}, 0, 0, 0, 0, 0) - {}_g\tilde{F}_x(0, 0, 0, 0, 0, 0))/(\delta\, {}_g\dot{x})$, with a sufficiently small $\delta\, {}_g\dot{x}$.

https://doi.org/10.1017/jfm.2021.68 Published online by Cambridge University Press

For hovering with the wing kinematics as shown in figure 2, D and W are expressed as

$$\left.\begin{aligned} D &= \begin{pmatrix} -4.47 & 2.28 & -5.99 \\ -0.15 & -9.37 & -0.69 \\ -10.7 & 3.62 & -31.2 \end{pmatrix} \times 10^{-4}, \\ W &= \begin{pmatrix} 0.29 & -0.45 & 6.55 \\ 7.71 & 0.00 & -1.24 \\ 1.66 & -7.36 & 9.84 \end{pmatrix} \times 10^{-4}. \end{aligned}\right\} \tag{6.6}$$

It can be seen from D that the pitch velocity has a significant effect on the forward/backward acceleration and, reversely, the forward/backward velocity also has an effect on the pitch acceleration. According to (6.4), the motion can be controlled by tuning the wing kinematics $\Delta\Phi$, $\Delta\bar{\varphi}$ and $\Delta\bar{\eta}$. Inspection of the matrix W reveals that the forward/backward motion is mainly controlled by the mean feathering angle, vertical motion is mainly controlled by the amplitude of the positional angle, and the body pitching motion is sensitive to both the mean positional angle and the mean feathering angle. With an objective of implementing a practical control strategy that would enable our bumblebee model to maintain hovering, we first introduce a transformation matrix P which helps to decouple the dynamical system by diagonalizing the damping matrix

$$PDP^{-1} = \Lambda = \begin{pmatrix} \lambda_1 & 0 & 0 \\ 0 & \lambda_2 & 0 \\ 0 & 0 & \lambda_3 \end{pmatrix}, \tag{6.7}$$

where

$$\lambda_1 = -3.2 \times 10^{-3}, \quad \lambda_2 = -2.2 \times 10^{-4}, \quad \lambda_3 = -9.1 \times 10^{-4} \tag{6.8}$$

and

$$P = \begin{pmatrix} -0.21 & -0.93 & 0.15 \\ 0.00 & 0.01 & -0.95 \\ -0.98 & 0.36 & -0.28 \end{pmatrix}. \tag{6.9}$$

With a change of variables $(\xi_1, \xi_2, \xi_3)' = P({}_gx, {}_gz, \beta)'$, (6.4) takes the form

$$\begin{pmatrix} \ddot{\xi}_1 \\ \ddot{\xi}_2 \\ \ddot{\xi}_3 \end{pmatrix} = \begin{pmatrix} \lambda_1\dot{\xi}_1 \\ \lambda_2\dot{\xi}_2 \\ \lambda_3\dot{\xi}_3 \end{pmatrix} + \begin{pmatrix} \Delta p_1 \\ \Delta p_2 \\ \Delta p_3 \end{pmatrix}, \tag{6.10}$$

where

$$\begin{pmatrix} \Delta p_1 \\ \Delta p_2 \\ \Delta p_3 \end{pmatrix} = PW \begin{pmatrix} \Delta\Phi \\ \Delta\bar{\varphi} \\ \Delta\bar{\eta} \end{pmatrix}. \tag{6.11}$$

If, in addition, for any i $(i = 1, 2, 3)$, Δp_i is set to be a function of ξ_i only, then the system is transformed from a MIMO (multi-input-multi-output) system into three SISO (single-input-single-output) systems.

It has been shown that insects exert control with a certain time delay (Dyhr *et al.* 2013). Here we set the time delay to be the period of one stroke cycle $T = 1/f$. The following PD

https://doi.org/10.1017/jfm.2021.68 Published online by Cambridge University Press

feedback controller is adopted,

$$\Delta p_i(t) = -k_i[\xi_i(t-T) + \tau_i \dot{\xi}_i(t-T)], \quad i = 1, 2, 3. \tag{6.12}$$

After substituting (6.12) into (6.10), we obtain

$$\ddot{\xi}_i(t) = \lambda_i \dot{\xi}_i(t) - k_i[\xi_i(t-T) + \tau_i \dot{\xi}_i(t-T)], \quad i = 1, 2, 3. \tag{6.13}$$

The next step is to find the optimal control parameters k_i and τ_i that would guarantee the fastest return to the equilibrium state. The Laplace transform on (6.13) with $\Xi_i(s) = \mathcal{L}[\xi_i(t)]$ writes as

$$\Xi_i(s) = \frac{\dot{\xi}_i(0) + (s - \lambda_i + k_i\tau_i\, \mathrm{e}^{-Ts})\xi_i(0)}{s^2 - \lambda_i s + k_i(1 + \tau_i s)\, \mathrm{e}^{-Ts}}, \quad i = 1, 2, 3. \tag{6.14}$$

If the exponential e^{-Ts} is approximated using the Padé approximant of order $(2, 2)$ (Franklin, Powell & Emami-Naeini 2014), (6.14) reduces to a polyrational fraction with its denominator to be a biquadratic polynomial which can be simplified as a sum of four partial fractions (Franklin *et al.* 2014). Performing the inverse Laplace transform, we obtain

$$\xi_i(t) = \sum_{j=1}^{4} c_{i,j}\, \mathrm{e}^{p_{i,j}t}, \quad i = 1, 2, 3, \tag{6.15}$$

where $(p_{i,1}, p_{i,2}, p_{i,3}, p_{i,4})$ are the poles (zeros of the denominator of (6.14)). Here $(c_{i,1}, c_{i,2}, c_{i,3}, c_{i,4})$ is dependent on the initial condition. Since ξ_i can grow or decay in time exponentially, the system (6.4) or (6.10) is stable if and only if the real part is negative for all poles, that is, $\mathcal{R}(p_{i,1}) < 0$, $\mathcal{R}(p_{i,2}) < 0$, $\mathcal{R}(p_{i,3}) < 0$, $\mathcal{R}(p_{i,4}) < 0$. If the system is stable, the time needed for the system to restore to equilibrium is determined by $p_{i,o} = \max\{\mathcal{R}(p_{i,1}), \mathcal{R}(p_{i,2}), \mathcal{R}(p_{i,3}), \mathcal{R}(p_{i,4})\}$ which corresponds to the slowest time decay. Hence, our goal to realize fastest return to the equilibrium reduces to finding the values of k_i and τ_i that minimize $p_{i,o}$, i.e.

$$\min_{k_i, \tau_i}\{p_{i,o}\}, \quad i = 1, 2, 3, \tag{6.16}$$

which is divided into two procedures. Firstly, we approximate the denominator of (6.14) in the form

$$1 + k_i \frac{1 + \tau_i s}{s^2 - \lambda_i s} \frac{1 - Ts/2 + (Ts)^2/12}{1 + Ts/2 + (Ts)^2/12} = 0, \quad i = 1, 2, 3, \tag{6.17}$$

and fix τ_i, applying the root locus method with respect to k_i. The root locus method is a graphical analysis that shows how the change of a parameter of a system affects the system's dynamic response. The method was first developed by Evans (1948) who gave rules for plotting the paths of the roots, a plot he called the root locus. The roots $(p_{i,1}, p_{i,2}, p_{i,3}, p_{i,4})$ of (6.17) can be clearly illustrated by the locus plot which helps to find the optimized $p_{i,o}$. Secondly, we vary τ_i, then the optimized $p_{i,o}$ with respect to τ_i can be obtained, which is the solution of the optimization problem (6.16). We take $i = 3$ as an example to show how to solve (6.16). For a given τ_3, there exist four root loci (corresponding to $p_{3,1}, p_{3,2}, p_{3,3}, p_{3,4}$) starting from $k_3 = 0(\times)$ to $k_3 \to +\infty(\circ)$; see figure 20. For small τ_3, $p_{3,o}$ is minimized when three roots $p_{3,1}, p_{3,2}, p_{3,3}$ have the same real part; see figure 20(*a*). With the increase of τ_3, $p_{3,o}$ becomes smaller until $p_{3,1}, p_{3,2}, p_{3,3}$ merge in one point, figure 20(*b*). As shown in figure 20(*c*) for large τ_3, when

https://doi.org/10.1017/jfm.2021.68 Published online by Cambridge University Press

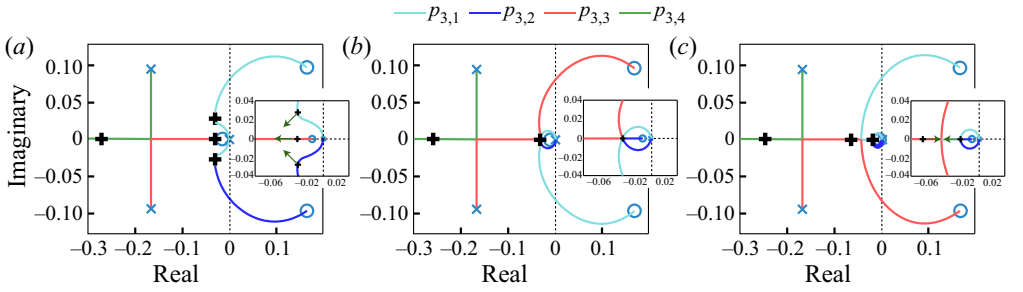


Figure 20. Root locus. (*a*) Plot for $\tau_3 = 80.13$. The arrows in the small figure indicate the variation of $p_{3,1}$, $p_{3,2}$ and $p_{3,3}$ with increasing τ_3. Plots for (*b*) $\tau_3 = 100.13$ and (*c*) $\tau_3 = 120.13$. The arrows in the small figure indicate the variation of $p_{3,1}$, $p_{3,2}$ and $p_{3,3}$ with decreasing τ_3. Here $\times$ and $\circ$ indicate that k_3 equals 0 and $+\infty$, respectively.

k_1	τ_1	k_2	τ_2	k_3	τ_3
2.79×10^{-4}	89.24	2.46×10^{-4}	103.79	2.53×10^{-4}	100.13

Table 9. Optimal control parameters of PD control.

$p_{1,1}p_{1,2}p_{1,3}$	$p_{1,4}$	$p_{2,1}, p_{2,2}, p_{2,3}$	$p_{2,4}$	$p_{3,1}, p_{3,2}, p_{3,3}$	$p_{3,4}$
−0.034	−0.258	−0.033	−0.261	−0.033	−0.260

Table 10. Poles corresponding to optimal control parameters for time delay of one stroke cycle.

two roots $p_{3,1}, p_{3,2}$ meet at the same point on the real axis, $p_{3,o}$ reaches minimum. With decreasing τ_3, $p_{3,o}$ becomes smaller until $p_{3,1}, p_{3,2}, p_{3,3}$ merge as shown in figure 20(*b*). Thus, the optimized $p_{3,o}$ for (6.16) is obtained. The corresponding k_i and τ_i are shown in table 9 and the corresponding poles $p_{i,j}$ are shown in table 10. Combining (6.11) and (6.12) and using the definition of ξ_i, we obtain an explicit expression for the control strategy,

$$\begin{pmatrix} \Delta\Phi \\ \Delta\bar{\varphi} \\ \Delta\bar{\eta} \end{pmatrix} = -W^{-1}P^{-1} \begin{pmatrix} k_1 & 0 & 0 \\ 0 & k_2 & 0 \\ 0 & 0 & k_3 \end{pmatrix} \left[P \begin{pmatrix} {}_g x \\ {}_g z \\ \beta \end{pmatrix} + \begin{pmatrix} \tau_1 & 0 & 0 \\ 0 & \tau_2 & 0 \\ 0 & 0 & \tau_3 \end{pmatrix} P \begin{pmatrix} {}_g \dot{x} \\ {}_g \dot{z} \\ \dot{\beta} \end{pmatrix} \right]. \quad (6.18)$$

To evaluate the performance of the PD control strategy derived using CDAM, we integrate it into the CFD environment and compare the results with those in the CDAM environment with the governing time-accurate dynamic equations from Sun *et al.* (2007) embedded. We first conduct system identification (Fei *et al.* 2019*a*) to fine-tune the hovering wing kinematics for CDAM and for CFD. For the default wing motion shown in figure 2, CDAM and CFD produce slightly different values for the forces and torques. For that reason, free flight simulation with the default wing kinematics would slightly deviate from hovering in a CDAM environment. To eliminate this deviation, the system identification is conducted by adding small offsets to the wing kinematics, i.e. positional amplitude offset ($\delta\Phi$), mean positional angle offset ($\delta\bar{\varphi}$) and mean feathering angle offset ($\delta\bar{\eta}$). The method to obtain the $\delta\Phi$, $\delta\bar{\varphi}$ and $\delta\bar{\eta}$ is the one adopted in § 5. The results are $\delta\Phi = -0.02$, $\delta\bar{\varphi} = 1.71^\circ$ and $\delta\bar{\eta} = -0.60^\circ$. Then, we apply the control strategy (6.18) in both CDAM and CFD environments, with the same values of k_i, τ_i and P-matrix.

https://doi.org/10.1017/jfm.2021.68 Published online by Cambridge University Press

The bumblebee is set in an initial state with nose up motion: $\dot{\beta}(0) = 285.52\,\mathrm{deg\ s^{-1}}$, ${}_g v_x(0) = 6.1\,\mathrm{m\ s^{-1}}$, ${}_g v_z(0) = 4.5\,\mathrm{m\ s^{-1}}$, $\beta(0) = 45\,\mathrm{deg}$, ${}_g x(0) = 0\,\mathrm{mm}$, ${}_g z(0) = 0\,\mathrm{mm}$. In the control process in the CFD environment, the bumblebee is fixed to flap its wings for three stroke cycles to make the surrounding flow fully developed. Then the bumblebee is released to perform free flying for one stroke cycle before applying control. In the control process in CDAM, the bumblebee is immediately released to perform free flying for one stroke cycle before activating the controls.

Figure 21 shows the time evolution of the position and pitch angle of the bumblebee during the recovery transition. It can be seen that the PD control strategy is successful in both the CDAM and CFD environments. The maximal values of the forward/backward position deviation and pitch angle are similar in both environments. For the vertical position, the fluctuation amplitude in CFD is larger. Note that, in the position control, the deviation during the whole control process is smaller than the mean chord length (4.1 mm). At the same time, deviation of pitch angle is as large as 5°.

It is difficult to know the exact time delay of one species. For instance, it is in the range of 2.6–6.7 ms for fruit flies' roll control (Beatus, Guckenheimer & Cohen 2015), 5–7.5 ms for blow flies (Hengstenberg *et al.* 1986). Here, we study the effect of time delay on the control parameters k and τ and thereby the restoring time. Figure 22(a) shows that both proportion gain and differentiation gain decrease with increment of time delay. The restoring behaviour of the system is described by (6.15) of which the $p_{i,j}$ with maximal real number determines the restoring time. After $-1/p_{i,j}$ from starting, the disturbance is decreased to $1/e$ of the original disturbance. Here, we treat $-1/p_{i,j}$ as the characteristic restoring time. From figure 22(b), the characteristic restoring time rises with the increment of time delay linearly.

The smallness of the positional deviation and similarity between the trends in the two environments demonstrate the effectiveness of the PD control strategy with the parameters determined using CDAM. This leads us to a twofold conclusion. Firstly, CDAM provides an effective tool for designing controllers that can then be used in more costly, but more predictive, CFD simulations. Secondly, to some extent, CDAM can successfully replace the CFD simulation to reduce the computation time. Other more complex control strategies like fuzzy control and reinforcement learning-based control can be designed with the aid of CDAM, which may be a promising perspective for future work.

7. Computational fluid dynamics data-driven aerodynamic model on the hawkmoth manduca

The leading edge vortex is the main contributor to the force generation. It can become unstable and tends to detach from the leading edge (Liu & Aono 2009). The shedding of the leading edge vortex in turn causes a reduction of force (Nakata *et al.* 2015) and limits the accuracy of the quasi-steady model. The hawkmoth flaps its large wings at a high Reynolds number (around 6000 in hovering) which lies within the border between insects and birds. Here we apply the proposed CDAM on the hawkmoth to test its limits at high Reynolds number.

The morphology parameters of the hawkmoth are borrowed from Willmott & Ellington (1997); see table 11. Wing kinematics of the hovering hawkmoth is shown in figure 23. As mentioned in § 2, we ran CFD cases at different velocities shown in table 12 and for each velocity, several CFD cases are run with different wing kinematics as can be seen in table 13, to obtain training data. To test the accuracy and generality of the quasi-steady model for flapping wings and the simplified aerodynamic model for a moving body,

https://doi.org/10.1017/jfm.2021.68 Published online by Cambridge University Press

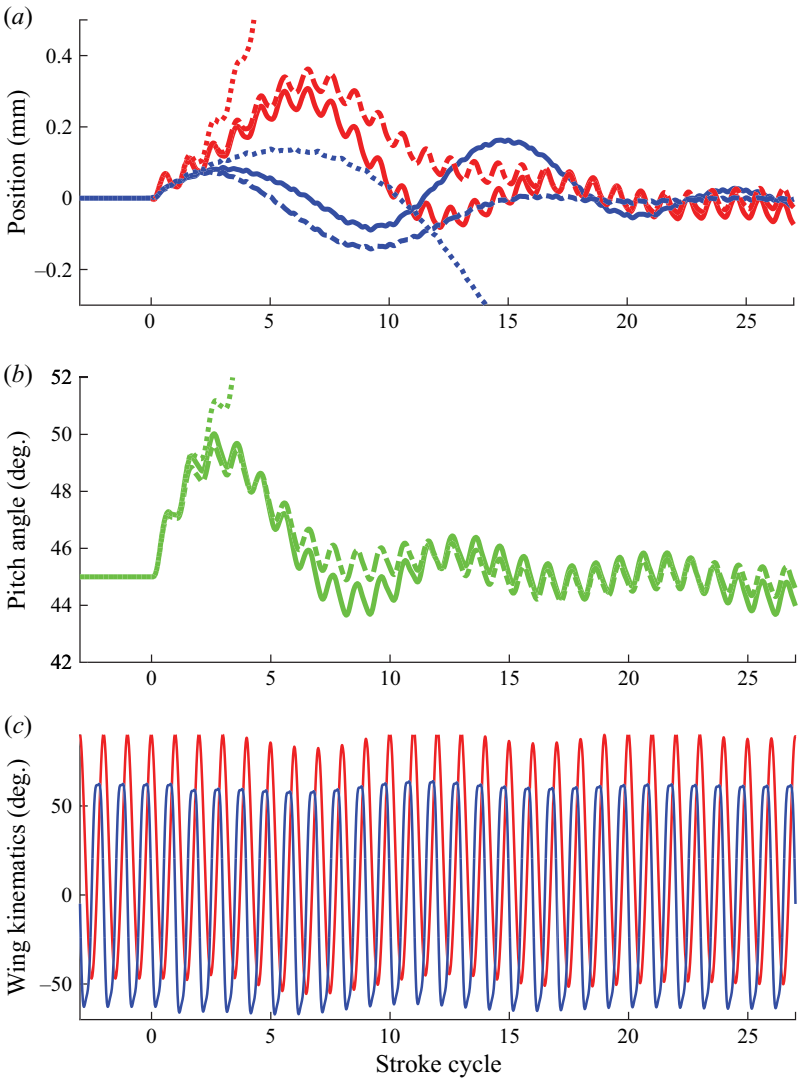


Figure 21. Longitudinal control process. (*a*) Position control and (*b*) pitch angle. Blue: vertical position; red: forward/backward position; green: pitch angle. Solid line: prediction by CFD; dashed line: prediction by the quasi-steady model; dotted line: uncontrolled. (*c*) Variation of wing kinematics during the control process. Red line: positional angle. Blue line: feathering angle.

10 more CFD cases with randomly selected flight velocities and wing kinematics are run, so called test data set; see table 14. Figure 24 shows a comparison between the quasi-steady model and CFD results. Figure 25 shows a comparison between the simplified aerodynamic model and CFD results. The predictions by the proposed model agree with the CFD results qualitatively well, but the discrepancy is larger than in the bumblebee case. Figure 26 shows the aerodynamics of the wing during upstroke in hovering. A horseshoe vortex begins to form at the onset of the upstroke, however, the leading edge vortex immediately sheds from the leading edge and a new leading edge vortex begins to form, which causes a decrease of force generation. During the shedding of the first leading edge vortex and generation of the second leading edge vortex, the quasi-steady

https://doi.org/10.1017/jfm.2021.68 Published online by Cambridge University Press

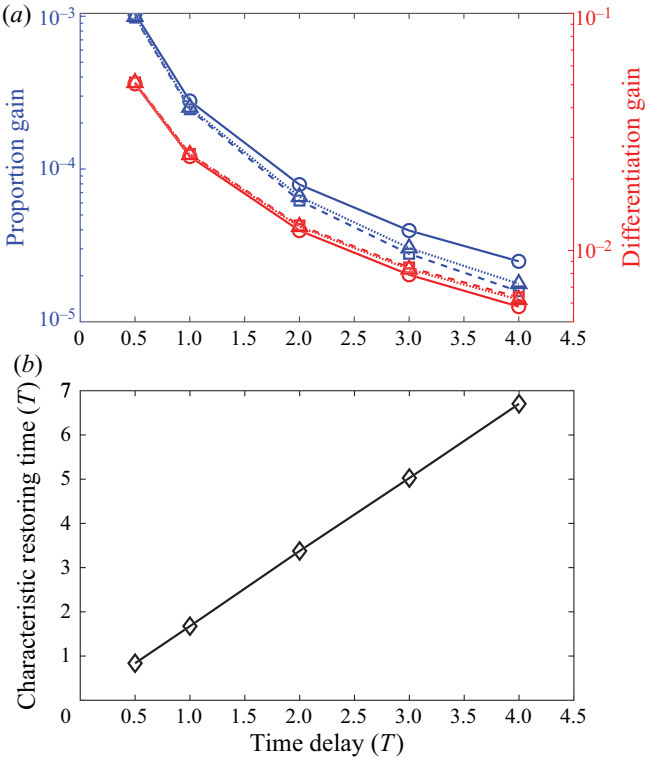


Figure 22. (*a*) Proportion gain k (blue) and differentiation gain $k\tau$ (red) over time delay. Solid line with circle: SISO system with damping effect λ_1. Dashed line with square: SISO system with damping effect λ_2. Dotted line with upper triangle: SISO system with damping effect λ_3. (*b*) Characteristic restoring time over time delay. Here T represents the stroke period 7.35×10^{-3} s.

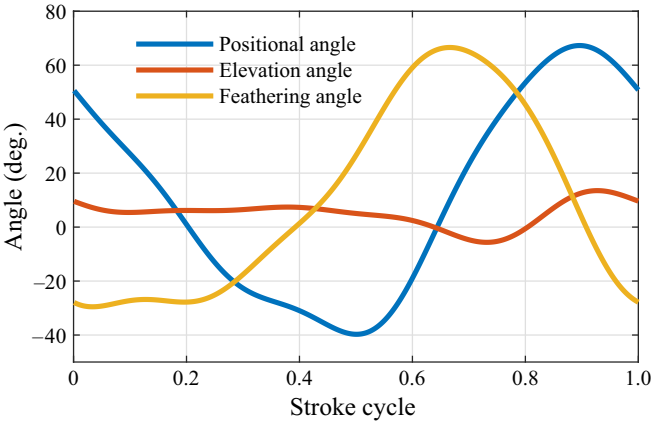


Figure 23. Wing kinematics of a hovering hawkmoth.

model overestimates the force production. In conclusion, the CDAM can be generalized to the hawkmoth with a small reduction in accuracy due to the unsteadiness of leading edge vortex.

https://doi.org/10.1017/jfm.2021.68 Published online by Cambridge University Press

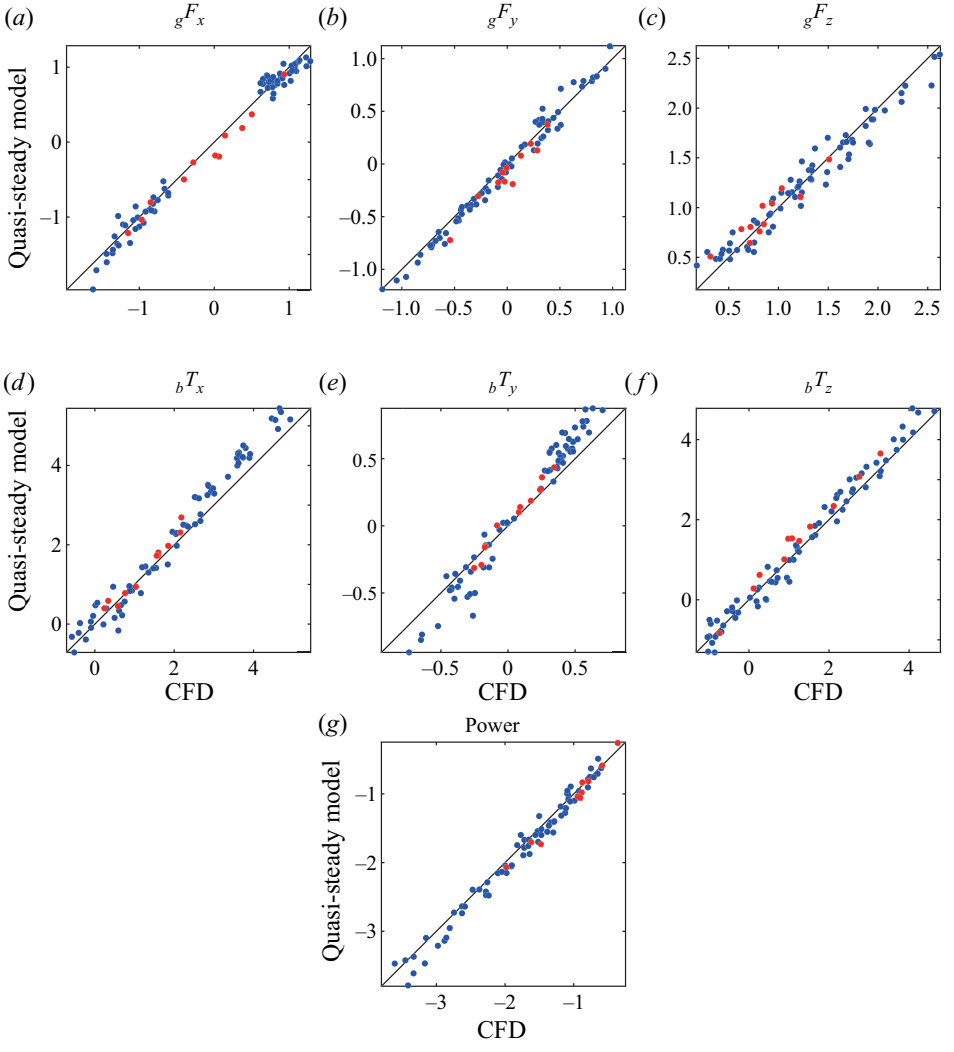


Figure 24. Comparison between the prediction of the quasi-steady model and CFD database for a flapping wing. (*a–c*) Aerodynamic forces in the ground frame, non-dimensionalized by $\rho U_{ref}^2 c_m^2$. (*d–f*) Aerodynamic torques with respect to the centre of body mass of a modelled hawkmoth in the body-fixed frame, non-dimensionalized by $\rho U_{ref}^2 c_m^3$. (*g*) Aerodynamic power consumptions, non-dimensionalized by $\rho U_{ref}^3 c_m^2$. Blue: training database. Red: test database. The solid line represents the equality of prediction of the quasi-steady model and CFD results.

8. Limitations on the current model

In § 2 we assumed that the aerodynamic force is normal to the wing surface and its centre is located on the rotation axis. We calculate the contribution of the aerodynamic force components in the wing plane for all the CFD database with various motions and wing kinematics, which turn out to be $3.5\,\% \pm 1.8\,\%$ of the total aerodynamic force, so the aerodynamic force is mainly normal to the wing surface. The aerodynamic torque with respect to the wing hinge normal to the plane is induced by the aerodynamic force

https://doi.org/10.1017/jfm.2021.68 Published online by Cambridge University Press

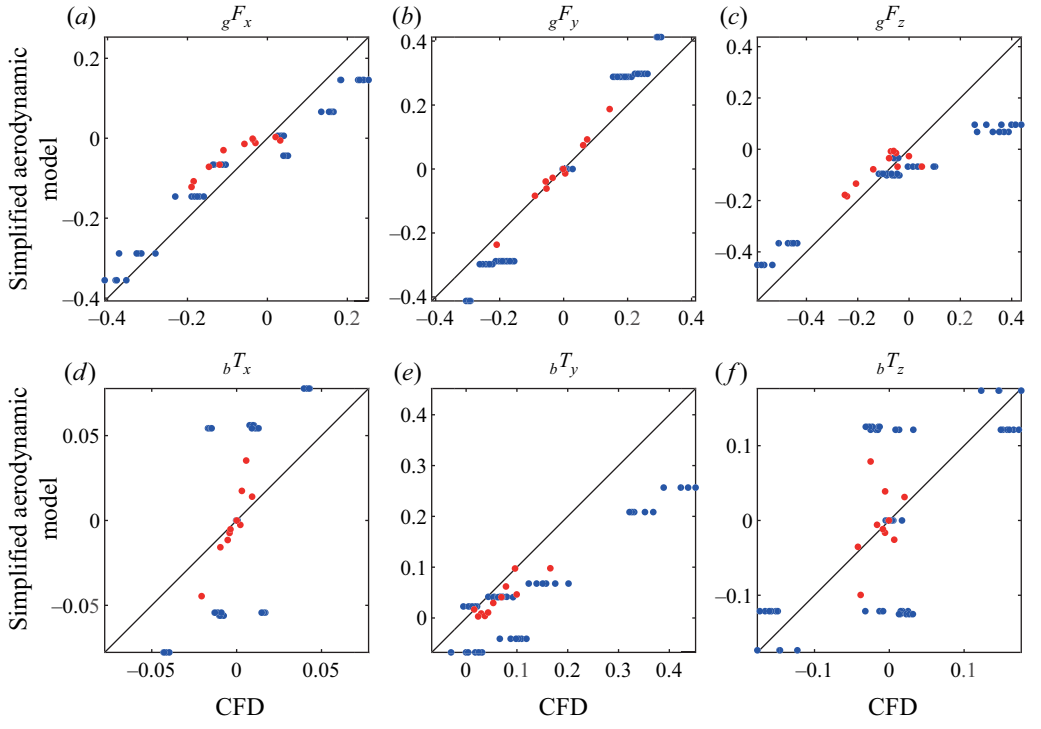


Figure 25. Comparison between the prediction of the simplified aerodynamic model and CFD database for a moving body. (*a–c*) Aerodynamic forces in the ground frame, non-dimensionalized by $\rho U_{ref}^2 c_m^2$. (*d–f*) Aerodynamic torques with respect to the centre of body mass of a modelled hawkmoth in the body-fixed frame, non-dimensionalized by $\rho U_{ref}^2 c_m^3$. Blue: training database. Red: test database. The solid line represents the equality of prediction of the simplified aerodynamic model and CFD results.

m_b	Body mass	1995 mg
m_w	Wing mass	45 mg
m_t	Mass of hawkmoth ($m_b + 2m_w$)	2085 mg
$_bI_{yy}$	Moment of inertia of body	5.25×10^{-8} kg m^2
R	Wing length	50.64 mg
$_b\boldsymbol{R}_h$	Location of wing base	$(-8.7, 7.6, 0)'$ mm
c_m	Man chord length	18.92 mm
f	Flapping frequency	25.4 Hz
Φ	Flapping amplitude	113 deg.
U_{ref}	Reference velocity ($2\Phi Rf$)	5.08 m s^{-1}

Table 11. Morphology of hawkmoth.

components in the wing plane, so its contribution to the total aerodynamic torque is also small, about 2.8 % ± 1.6 %.

The spanwise aerodynamic torque, also called pitching torque, is comparatively large especially near stroke reversal as shown in figure 4. The pitching torque is due to the aerodynamic force component normal to the wing surface along with its location from the rotation axis. Dickson *et al.* (2006) experimentally found a linear relationship between

https://doi.org/10.1017/jfm.2021.68 Published online by Cambridge University Press

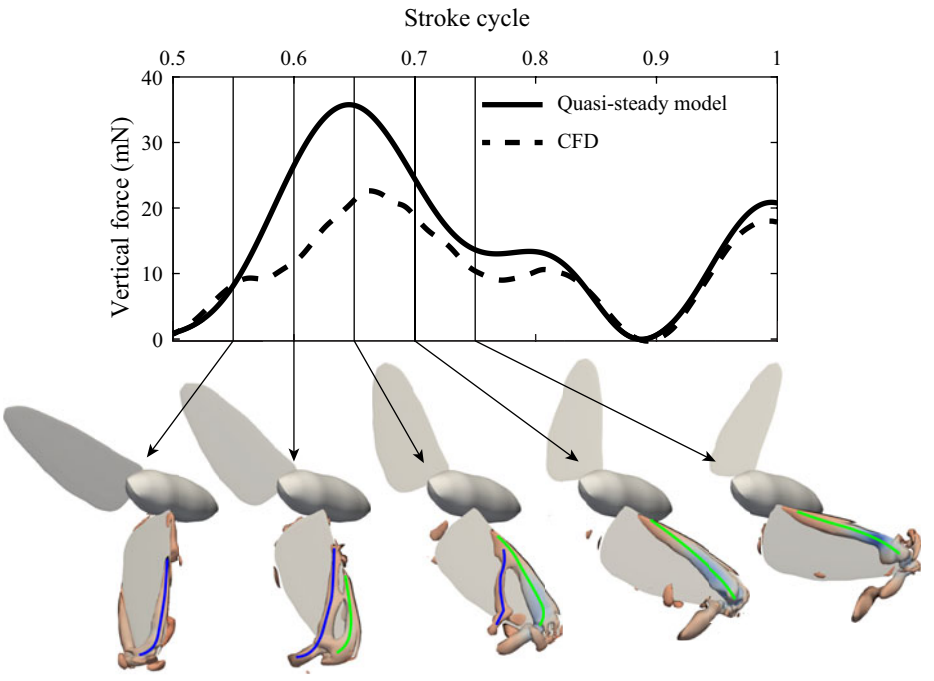


Figure 26. Aerodynamics of a hovering hawkmoth. The blue curve indicates the first generated leading edge vortex. The green curve indicates the second generated leading edge vortex.

No.	Forward/backward (U_{ref})	Lateral (U_{ref})	Vertical (U_{ref})
1	−0.4	0	0
2	−0.4	0	0.4
3	−0.4	0.4	0
4	−0.4	−0.4	0
5	−0.4	0.4	0.4
6	−0.4	−0.4	0.4
7	0.4	0	0
8	0.4	0	0.4
9	0.4	0.4	0
10	0.4	−0.4	0
11	0.4	0.4	0.4
12	0.4	−0.4	0.4

Table 12. Adopted flight velocities of modelled hawkmoth for training data set.

the location of the aerodynamic force and the angle of attack for the fruit fly *Drosophila melanogaster*. According to figure 4, the pitching torque is around zero except for the stroke reversal which means the location of aerodynamic force is near the rotation axis. During stroke reversals when the angle of attack is near $\pi/2$, the location of aerodynamic force moves away from the rotation axis, therefore, the pitching torque becomes larger. However, the stroke reversal lasts for a short time and the pitching torque changes sign during stroke reversal, so the pitching torque has a minor effect on the overall aerodynamic torque production. Hereby, in this paper, the pitching torque is not considered. It should

https://doi.org/10.1017/jfm.2021.68 Published online by Cambridge University Press

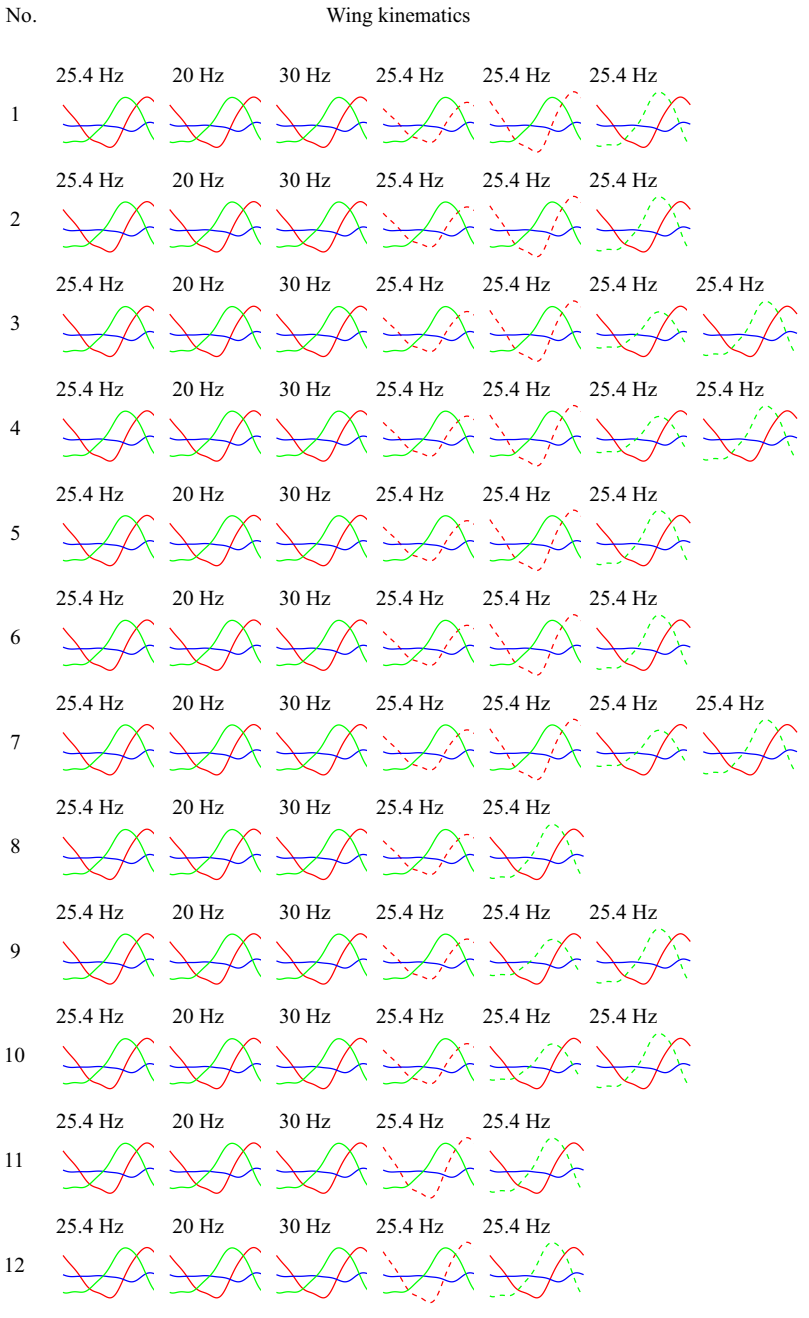


Table 13. Adopted wing kinematics of modelled hawkmoth for training data set. The row numbers are corresponding to those in table 12.

https://doi.org/10.1017/jfm.2021.68 Published online by Cambridge University Press

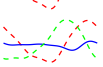
No.	Forward/backward (U_{ref})	Lateral (U_{ref})	Vertical (U_{ref})	Frequency (Hz)	Wing kinematics
1	0.258	−0.179	0.14	21.29	
2	0.155	0.143	0.332	25.68	
3	−0.146	0.124	0.234	24.69	
4	−0.372	−0.304	0.366	23.37	
5	−0.049	−0.001	0.114	21.62	
6	−0.094	0.367	0.302	27.94	
7	0.212	−0.127	0.301	23.11	
8	0.236	0.068	0.152	25.28	
9	−0.25	−0.22	0.227	21.65	
10	−0.008	0.201	0.03	26.01	

Table 14. Adopted flight velocities and wing kinematics of modelled hawkmoth for test data set.

be noted that the chordwise location of aerodynamic force affects the pitching torque around the rotation axis which does play a crucial role in analysing and designing micro air vehicles (MAVs) with passive feathering wings (Whitney & Wood 2010), which is not considered in this paper. In addition, for certain wings with extreme morphology, for instance, a wing with the rotation axis located on the leading edge, the pitching torque becomes non-negligible. Further work will be focused on solving this potential limitation.

The proposed model calculates the aerodynamic force for the wings and body separately. The interactions between them are not captured, which may underestimate the aerodynamic force. There are two outliers (marked in table 4) of the least square error of the force normal to the wing surface; see figure 6(*a*). The modelled bumblebee corresponding to the two outliers move leftward. In such case, the inflow is disturbed by the left wing and the body before it interacts with the right wing. Such an unsteady effect is not captured by the current model.

9. Conclusion

In this paper we proposed a versatile CDAM for fast while precise evaluation of aerodynamic performance in insect flight, which comprises a quasi-steady model for flapping wings and a simplified aerodynamic model for a moving body, demonstrating potential capabilities in various flight behaviours of forward and backward flight, lateral (sideslip) flight as well as ascending flight. The CDAM is verified to be capable of achieving an accurate estimation of flapping aerodynamic loads over a broad range of longitudinal, lateral and vertical velocities with various wing kinematics. Unsteady aerodynamic effects are accounted for by fitting the parameterizing coefficients using

https://doi.org/10.1017/jfm.2021.68 Published online by Cambridge University Press

CFD-based results; the accuracy and generalization are demonstrated through comparing with a CFD database involving a training data set and a test data set. The CFD training data set is utilized to inform the parameterized CDAM through minimizing the least square error and the coefficients are then generalized to arbitrary flying velocity by means of a surrogate model. The CFD test data set is employed to validate the CDAM-based computations, indicating reasonable agreement between the CDAM-based and CFD-based estimation of the aerodynamic force, torque and power at various flying velocities while achieving reasonable consistency between the CFD-training and test data sets. Our results demonstrate that the CDAM developed here establishes an efficient aerodynamic model to achieve accurate evaluation of flapping aerodynamic performance for the objective bumblebee model but not limited to it at arbitrary flying velocities. It is worth noting that this novel aerodynamic model can be easily applied to other insect models and even insect-inspired flapping MAVs under the same framework.

Generally, data-driven models are precise when used in the range covered by the training data. Physics-based models are accurate when the underlying physical assumptions are valid, and they do not require training data. It is common to have distinct models of these two kinds coupled in multi-physics simulations. However, our situation is different: the proposed aerodynamic model is, at the same time, physics-based with adjustable parameters and data driven with physically intuitive interpolation functions. The parameter identification is achieved by a computationally intense process of numerical optimization, yet it is much less costly than the CFD simulation. By tuning the parameters we partly compensate for the crudeness of the physical model, while the fact of having a physical model partly compensates for the limited amount of training data.

We further developed a genetic algorithm-based optimization method (Hansen *et al.* 2003; Hansen & Kern 2004) embedded with the CDAM, which is proven to be fast and efficient in examining the trimmed states for the forward flying bumblebee model with adjustment of wing kinematics. We found that for a specific forward flight velocity, the trim states based on the method are multiple and not unique, implying that bumblebees can quickly settle to the nearest trimmed state starting from an arbitrary initial condition. Interestingly, our model predicts an apparently linear correlation between body angle, stroke plane angle and aerodynamic power, which is also observed in bumblebee flights (Dudley & Ellington 1990*a*,*b*), but the latter displays a relatively lower power consumption. This suggests that bumblebees likely select some trimmed state with the minimal power consumption. Besides wing kinematics (Combes *et al.* 2020), body attitudes (body angle and stroke plane angle) can also affect the power consumption, which however has not been explored yet and would be our future work.

The CDAM characterized by an analytical expression can be easily combined with the flight dynamics of free-flying insects (Sun *et al.* 2007; Xiong & Sun 2008) and even flapping-wing MAVs to help design flight controllers (Fei *et al.* 2019*a*). For instance, given the flight dynamics expressed explicitly, it would be easier to derive the control parameters (Yao & Yeo 2019). With the aid of CDAM, here we further designed a longitudinal PD control strategy for stabilizing the bumblebee model in hovering. Coordinate transformation is implemented to decouple the three degrees of freedom in longitudinal directions so as to reduce the number of control parameters. Laplace transformation and the root locus method are employed to determine the optimized control parameters. The PD control works well and consistently in both CDAM and CFD environments. This indicates that the proposed methodology of CDAMs if trained with a sufficiently large CFD database covering a broad range of flying velocities in a three-dimensional space can be effective and robust enough to predict the unsteady aerodynamics in association with various maneuvering in flapping flights. Thus, as an

https://doi.org/10.1017/jfm.2021.68 Published online by Cambridge University Press

alternative to CFD modelling, the CDAM integrated with the sensorimotor mechanics (Tu & Dickinson 1996; Balint & Dickinson 2001; Dyhr *et al.* 2013) can be utilized to analyse how insects control flapping wings to achieve complex agile flights.

Further improvement of the CDAM's accuracy can be achieved by enhancing the CFD database by sub-discretizing the velocity space, and by adding more aerodynamic factors related with the key parameters such as the Reynolds number and the Rossby number (Lee *et al.* 2016), as well as by introducing the deep learning method. Moreover, potential applications of the CDAM may cover various aspects in association with complex maneuverability and flight control in insect-inspired flight systems for both biological flyers (insects) and bioinspired flapping MAVs.

Supplementary material. Supplementary material is available at https://doi.org/10.1017/jfm.2021.68.

Acknowledgements. X.C. acknowledges the Excellent International Student Scholarship provided by Chiba University.

Funding. This work was supported by the Japan Society for the Promotion of Science (JSPS) (KAKENHI No. 19H02060 and No. 18K13693).

Declaration of interests. The authors report no conflict of interest.

Author ORCIDs.
Dmitry Kolomenskiy https://orcid.org/0000-0003-0107-6894;
Toshiyuki Nakata https://orcid.org/0000-0002-0378-2242;
Hao Liu https://orcid.org/0000-0002-8687-3237.

Appendix A. Derivation of the terms of quasi-steady model

Translational circulation due to the translation of the wing element is (Berman & Wang 2007)

$$\Gamma_{trans}(r) = -\tfrac{1}{2} C_T \sin 2\alpha c(r)|_w v_{wn}|, \tag{A1}$$

so the lift due to translational circulation is

$$f_{tc}(r) = \rho \Gamma_{trans}(r)|_w v_{wn}|, \tag{A2}$$

which is normal to the translation velocity of the wing element. Taking the component normal to the wing surface of (A2) we get (2.10).

Rotational circulation due to the rotation of the wing element is (Pesavento & Wang 2004; Berman & Wang 2007)

$$\Gamma_{rot} = -\tfrac{1}{2} C_R \dot{\eta} c^2(r), \tag{A3}$$

so the lift due to rotational circulation is

$$f_{rc}(r) = \rho \Gamma_{rot}(r)|_w v_{wn}|, \tag{A4}$$

which is normal to the translation velocity of the wing element. Taking the component normal to the wing surface of (A4) we get (2.11).

The formulation of translational drag is adopted from Wang (2004) and Berman & Wang (2007),

$$f_{td}(r) = -\frac{1}{2}\rho c(r)\left[C_D(0)\cos^2\alpha + C_D\left(\frac{\pi}{2}\right)\sin^2\alpha\right]|_w v_w|^2, \tag{A5}$$

which acts in the opposite direction of the translation velocity of the wing element where $C_D(0)$ and $C_D(\pi/2)$ are translational drag coefficients with respect to the angle of attack

https://doi.org/10.1017/jfm.2021.68 Published online by Cambridge University Press

equal to 0 and $\pi/2$. Taking the component normal to the wing surface of (A5), we get

$$f_{td,N}(r) = -\frac{1}{2}\rho c(r)\left[C_D(0)\cos^2\alpha + C_D\left(\frac{\pi}{2}\right)\sin^2\alpha\right]|_w v_w|_w v_{w,z}. \tag{A6}$$

It can be found that the term related to $C_D(0)$ of (A5) and (2.10) have the same form, so without loss of generality, the term related to $C_D(0)$ of (A5) is merged into $f_{tc,N}(r)$ and $f_{tc,N}(r)$ keep the form as in (2.10). Then abbreviating $C_D(\pi/2)$ to C_D we get (2.12).

Equation (A5) is applied to describe the drag due to the translation motion of the wing element. When the wing element rotates around the rotation axis, additional drag due to rotation will be induced. This is because additional velocity $(-_w\omega_{w,y_w}x)$ of the point on the wing element is induced with respect to the rotation axis as shown in figure 3 which is normal to the wing surface. It is straightforward to adapt (A5) or (A6) to form the rotational drag (2.13) by integrating over the wing element

$$f_{rd,N} = -\frac{1}{2}\rho C_{rd}|\dot{\eta}|\dot{\eta}\int_{f_l}^{f_t}|x|x\,\mathrm{d}x. \tag{A7}$$

The added mass induced force (2.14) is adopted from Whitney & Wood (2010).

References

Andersen, A., Pesavento, U. & Wang, Z.J. 2005 Unsteady aerodynamics of fluttering and tumbling plates. *J. Fluid Mech.* **541**, 65–90.

Aono, H. & Liu, H. 2006 Vortical structure and aerodynamics of hawkmoth hovering. *J. Biomech. Sci. Engng* **1** (1), 234–245.

Balint, C.N. & Dickinson, M.H. 2001 The correlation between wing kinematics and steering muscle activity in the blowfly *Calliphora vicina*. *J. Expl Biol.* **204** (24), 4213–4226.

Beatus, T., Guckenheimer, J.M. & Cohen, I. 2015 Controlling roll perturbations in fruit flies. *J. R. Soc. Interface* **12** (105), 20150075.

Berman, G.J. & Wang, Z.J. 2007 Energy-minimizing kinematics in hovering insect flight. *J. Fluid Mech.* **582**, 153–168.

Bluman, J. & Kang, C.K. 2017 Wing-wake interaction destabilizes hover equilibrium of a flapping insect-scale wing. *Bioinspir. Biomim.* **12** (4), 046004.

Cheng, B., Fry, S.N., Huang, Q. & Deng, X. 2010 Aerodynamic damping during rapid flight maneuvers in the fruit fly drosophila. *J. Expl Biol.* **213** (4), 602–612.

Cheng, X. & Sun, M. 2018 Very small insects use novel wing flapping and drag principle to generate the weight-supporting vertical force. *J. Fluid Mech.* **855**, 646–670.

Combes, S.A., Gagliardi, S.F., Switzer, C.M. & Dillon, M.E. 2020 Kinematic flexibility allows bumblebees to increase energetic efficiency when carrying heavy loads. *Sci. Adv.* **6** (6), eaay3115.

Demoll, R. 1918 *Der Flug der Insekten und der Vögel: eine Gegenüberstellung*. G. Fischer.

Deng, X., Schenato, L. & Sastry, S.S. 2006 Flapping flight for biomimetic robotic insects: part II-flight control design. *IEEE Trans. Robot.* **22** (4), 789–803.

Dickinson, M.H., Lehmann, F. -O. & Sane, S.P. 1999 Wing rotation and the aerodynamic basis of insect flight. *Science* **284** (5422), 1954–1960.

Dickinson, M.H. & Muijres, F.T. 2016 The aerodynamics and control of free flight manoeuvres indrosophila. *Phil. Trans. R. Soc* B **371** (1704), 20150388.

Dickson, W.B. & Dickinson, M.H. 2004 The effect of advance ratio on the aerodynamics of revolving wings. *J. Expl Biol.* **207** (24), 4269–4281.

Dickson, W.B., Straw, A.D., Poelma, C. & Dickinson, M.H. 2006 An integrative model of insect flight control. *AIAA Paper* 2006-34.

Dudley, R. & Ellington, C.P. 1990*a* Mechanics of forward flight in bumblebees: I. Kinematics and morphology. *J. Expl Biol.* **148** (1), 19–52.

Dudley, R. & Ellington, C.P. 1990*b* Mechanics of forward flight in bumblebees: II. Quasi-steady lift and power requirements. *J. Expl Biol.* **148** (1), 53–88.

Dyhr, J.P., Morgansen, K.A., Daniel, T.L. & Cowan, N.J. 2013 Flexible strategies for flight control: an active role for the abdomen. *J. Expl Biol.* **216** (9), 1523–1536.

https://doi.org/10.1017/jfm.2021.68 Published online by Cambridge University Press

ELLINGTON, C.P. 1984 The aerodynamics of hovering insect flight. I. The quasi-steady analysis. *Phil. Trans. R. Soc. Lond.* B **305** (1122), 1–15.

ELLINGTON, C.P. & LIGHTHILL, M.J. 1984 The aerodynamics of hovering insect flight. IV. Aerodynamic mechanisms. *Phil. Trans. R. Soc. Lond.* B **305** (1122), 79–113.

ENGELS, T., KOLOMENSKIY, D., SCHNEIDER, K., LEHMANN, F.-O. & SESTERHENN, J. 2016*a* Bumblebee flight in heavy turbulence. *Phys. Rev. Lett.* **116** (2), 028103.

ENGELS, T., KOLOMENSKIY, D., SCHNEIDER, K. & SESTERHENN, J. 2016*b* FluSI: A novel parallel simulation tool for flapping insect flight using a fourier method with volume penalization. *SIAM J. Sci. Comput.* **38** (5), S3–S24.

EVANS, W.R. 1948 Graphical analysis of control systems. *IEEE* **67** (1), 547–551.

FEI, F., TU, Z., YANG, Y., ZHANG, J. & DENG, X. 2019*a* Flappy hummingbird: An open source dynamic simulation of flapping wing robots and animals. In *2019 International Conference on Robotics and Automation (ICRA)*, pp. 9223–9229.

FEI, F., TU, Z., ZHANG, J. & DENG, X. 2019*b* Learning extreme hummingbird maneuvers on flapping wing robots. In *2019 International Conference on Robotics and Automation (ICRA)*, pp. 109–115.

FRANKLIN, G.F., POWELL, J.D. & EMAMI-NAEINI, A. 2014 *Feedback Control of Dynamic Systems*. Prentice Hall.

FUNG, Y.C. 2008 *An Introduction to the Theory of Aeroelasticity*. Courier Dover Publications.

GLAUERT, H. 1983 *The Elements of Aerofoil and Airscrew Theory*. Cambridge University Press.

HANSEN, N. & KERN, S. 2004 *Evaluating the CMA Evolution Strategy on Multimodal Test Functions*, pp. 282–291. Springer.

HANSEN, N., MÜLLER, S.D. & KOUMOUTSAKOS, P. 2003 Reducing the time complexity of the derandomized evolution strategy with covariance matrix adaptation (CMA-ES). *Evol. Comput.* **11** (1), 1–18.

HEDRICK, T.L., CHENG, B. & DENG, X. 2009 Wingbeat time and the scaling of passive rotational damping in flapping flight. *Science* **324** (5924), 252–255.

HEDRICK, T.L. & DANIEL, T.L. 2006 Flight control in the hawkmoth *Manduca sexta*: the inverse problem of hovering. *J. Expl Biol.* **209** (16), 3114–3130.

HENGSTENBERG, R., SANDEMAN, D.C., HENGSTENBERG, B. & HORRIDGE, G.A. 1986 Compensatory head roll in the blowfly calliphora during flight. *Proc. R. Soc. Lond.* B **227** (1249), 455–482.

HOFF, W. 1919 Der flug der insekten und der Vögel. *Naturwissenschaften* **7**, 159–162.

ISHIHARA, D. 2018 Role of fluid-structure interaction in generating the characteristic tip path of a flapping flexible wing. *Phys. Rev.* E **98**, 032411.

JAKOBI, T., KOLOMENSKIY, D., IKEDA, T., WATKINS, S., FISHER, A., LIU, H. & RAVI, S. 2018 Bees with attitude: the effects of directed gusts on flight trajectories. *Biol. Open* **7** (10), bio034074.

JENSEN, M. & PRINGLE, J.W.S. 1956 Biology and physics of locust flight. III. The aerodynamics of locust flight. *Phil. Trans. R. Soc. Lond.* B **239** (667), 511–552.

KOLOMENSKIY, D., *et al.* 2019 The dynamics of passive feathering rotation in hovering flight of bumblebees. *J. Fluids Struct.* **91**, 102628.

LEE, Y.J., LUA, K.B., LIM, T.T. & YEO, K.S. 2016 A quasi-steady aerodynamic model for flapping flight with improved adaptability. *Bioinspir. Biomim.* **11** (3), 036005.

LENTINK, D. & DICKINSON, M.H. 2009 Rotational accelerations stabilize leading edge vortices on revolving fly wings. *J. Expl Biol.* **212** (16), 2705–2719.

LIU, G., DONG, H. & LI, C. 2016*a* Vortex dynamics and new lift enhancement mechanism of wing–body interaction in insect forward flight. *J. Fluid Mech.* **795** 634–651.

LIU, H. 2002 Computational biological fluid dynamics: digitizing and visualizing animal swimming and flying. *Integr. Compar. Biol.* **42** (5), 1050–1059.

LIU, H. 2009 Integrated modelling of insect flight: from morphology, kinematics to aerodynamics. *J. Comput. Phys.* **228** (2), 439–459.

LIU, H. & AONO, H. 2009 Size effects on insect hovering aerodynamics: an integrated computational study. *Bioinspir. Biomim.* **4** (1), 015002.

LIU, H., ELLINGTON, C.P., KAWACHI, K., VAN DEN BERG, C. & WILLMOTT, A.P. 1998 A computational fluid dynamic study of hawkmoth hovering. *J. Expl Biol.* **201** (4), 461–477.

LIU, H. & KAWACHI, K. 1998 A numerical study of insect flight. *J. Comput. Phys.* **146** (1), 124–156.

LIU, H., NAKATA, T., GAO, N., MAEDA, M., AONO, H. & SHYY, W. 2010 Micro air vehicle-motivated computational biomechanics in bio-flights: aerodynamics, flight dynamics and maneuvering stability. *Acta Mechanica Sin.* **26** (6), 863–879.

https://doi.org/10.1017/jfm.2021.68 Published online by Cambridge University Press

LIU, H., RAVI, S., KOLOMENSKIY, D. & TANAKA, H. 2016*b* Biomechanics and biomimetics in insect-inspired flight systems. *Phil. Trans. R. Soc.* B **371** (1704), 20150390.

LOPHAVEN, S.N., NIELSEN, H.B. & SØNDERGAARD, J. 2002 DACE – a Matlab Kriging toolbox, version 2.0. *Tech Rep*. Informatics and Mathematical Modelling, Technical University of Denmark, DTU, Richard Petersens Plads, Building 321, DK-2800 Kgs. Lyngby.

NABAWY, M.R.A. & CROWTHER, W.J. 2014 On the quasi-steady aerodynamics of normal hovering flight part II: model implementation and evaluation. *J. R. Soc. Interface* **11** (94), 20131197.

NAKATA, T., LIU, H. & BOMPHREY, R.J. 2015 A CFD-informed quasi-steady model of flapping-wing aerodynamics. *J. Fluid Mech.* **783**, 323–343.

NAKATA, T., LIU, H., TANAKA, Y., NISHIHASHI, N., WANG, X. & SATO, A. 2011 Aerodynamics of a bio-inspired flexible flapping-wing micro air vehicle. *Bioinspir. Biomim.* **6** (4), 045002.

NGUYEN, T.T., SHYAM SUNDAR, D., YEO, K.S. & LIM, T.T. 2016 Modeling and analysis of insect-like flexible wings at low Reynolds number. *J. Fluids Struct.* **62**, 294–317.

OH, S., LEE, B., PARK, H., CHOI, H. & KIM, S. 2020 A numerical and theoretical study of the aerodynamic performance of a hovering rhinoceros beetle (*Trypoxylus dichotomus*). *J. Fluid Mech.* **885**, A18.

OSBORNE, M.F.M. 1951 Aerodynamics of flapping flight with application to insects. *J. Expl Biol.* **28** (2), 221–245.

PESAVENTO, U. & WANG, Z.J. 2004 Falling paper: Navier–Stokes solutions, model of fluid forces, and center of mass elevation. *Phys. Rev. Lett.* **93** (14), 144501.

RAVI, S., KOLOMENSKIY, D., ENGELS, T., SCHNEIDER, K., WANG, C., SESTERHENN, J. & LIU, H. 2016 Bumblebees minimize control challenges by combining active and passive modes in unsteady winds. *Sci. Rep.* **6**, 35043.

SANE, S.P. & DICKINSON, M.H. 2002 The aerodynamic effects of wing rotation and a revised quasi-steady model of flapping flight. *J. Expl Biol.* **205** (8), 1087–1096.

SEDOV, L.I. 1965 *Two-dimensional Problems in Hydrodynamics and Aerodynamics*. Interscience.

SHYY, W., AONO, H., KANG, C. & LIU, H. 2013 *An Introduction to Flapping Wing Aaerodynamics*. Cambridge University Press.

SHYY, W., LIAN, Y., TANG, J., VIIERU, D. & LIU, H. 2007 *Aerodynamics of Low Reynolds Number Flyers*. Cambridge University Press.

SUN, M., WANG, J. & XIONG, Y. 2007 Dynamic flight stability of hovering insects. *Acta Mechanica Sin.* **23** (3), 231–246.

TU, M.S. & DICKINSON, M.H. 1996 The control of wing kinematics by two steering muscles of the blowfly (Calliphora vicina). *J. Compar. Physiol.* A **178** (6), 813–830.

USHERWOOD, J.R. & ELLINGTON, C.P. 2002 The aerodynamics of revolving wings II. Propeller force coefficients from mayfly to quail. *J. Expl Biol.* **205** (11), 1565–1576.

VAN DALSEM, W.R. & STEGER, J.L. 1986 Using the boundary-layer equations in three-dimensional viscous flow simulations. In *Proceedings of AGARD Fluid Dynamics Panel Symposium on Application of CFD in Aeronautics*, pp. 7–10.

VAN VEEN, W.G., VAN LEEUWEN, J.L. & MUIJRES, F.T. 2019 A chordwise offset of the wing-pitch axis enhances rotational aerodynamic forces on insect wings: a numerical study. *J. R. Soc. Interface* **16** (155), 20190118.

WANG, Q., GOOSEN, J.F.L. & VAN KEULEN, F. 2016 A predictive quasi-steady model of aerodynamic loads on flapping wings. *J. Fluid Mech.* **800**, 688–719.

WANG, Z.J. 2004 Unsteady forces and flows in low Reynolds number hovering flight: two-dimensional computations vs robotic wing experiments. *J. Expl Biol.* **207** (3), 449–460.

WEIS-FOGH, T. 1973 Quick estimates of flight fitness in hovering animals, including novel mechanisms for lift production. *J. Expl Biol.* **59** (1), 169–230.

WHITNEY, J.P. & WOOD, R.J. 2010 Aeromechanics of passive rotation in flapping flight. *J. Fluid Mech.* **660**, 197–220.

WILLMOTT, A.P. & ELLINGTON, C.P. 1997 The mechanics of flight in the hawkmoth manduca sexta. I. Kinematics of hovering and forward flight. *J. Expl Biol.* **200** (21), 2705–2722.

XIONG, Y. & SUN, M. 2008 Dynamic flight stability of a bumblebee in forward flight. *Acta Mechanica Sin.* **24** (1), 25–36.

YAO, J. & YEO, K.S. 2019 A simplified dynamic model for controlled insect hovering flight and control stability analysis. *Bioinspir. Biomim.* **14** (5), 056005.

YU, X. & SUN, M. 2009 A computational study of the wing–wing and wing–body interactions of a model insect. *Acta Mechanica Sin.* **25** (4), 421–431.

ZHANG, C., HEDRICK, T.L. & MITTAL, R. 2019 An integrated study of the aeromechanics of hovering flight in perturbed flows. *AIAA J.* **57** (9), 3753–3764.

https://doi.org/10.1017/jfm.2021.68 Published online by Cambridge University Press